TENSEGRITY STRUCTURES WITH EMBEDDED INERTIAL AMPLIFICATION MECHANISMS

by

Muhammet Nazım Açıcı

B.S., Mechanical Engineering and Physics, Boğaziçi University, 2020

Submitted to the Institute for Graduate Studies in

Science and Engineering in partial fulfillment of

the requirements for the degree of

Master of Science

Graduate Program in Mechanical Engineering

Boğaziçi University

2025

ACKNOWLEDGEMENTS

First of all, I would like to express my deepest gratitude to my thesis advisor Prof. Dr. Çetin Yılmaz for supervising me with patience, creative ideas, devotion and accessibility throughout my entire thesis duration. Without his motivation and wisdom, I would never have been able to commit myself to complete this project. I would like to thank him for endless support when I worked with him.

I would like to thank the members of my thesis committee Prof. Dr. Haluk Erol and Prof. Dr. Serdar Soyöz for giving their valuable time to read this thesis and giving crucial comments about it.

Finally, I would like to express my special appreciation to my beloved family and friends. My wife, Ezgi Turan, has given significant emotional support to finish my thesis. She always encouraged me when I felt exhausted. I owe her my most special thanks.

ABSTRACT

TENSEGRITY STRUCTURES WITH EMBEDDED INERTIAL AMPLIFICATION MECHANISMS

In this thesis, novel tensegrity structures with embedded inertial amplification mechanisms are designed to obtain wide and deep low frequency band gaps. Two different lever type tensegrity structures (LTTSs) are introduced, which has one lever or two levers in their unit cells. Analytical models of these two types of LTTSs are obtained. Vibration isolation performance of these unit cells is determined and compared with the band structure of one-dimensional periodic systems that use these unit cells. Parametric studies are conducted to see how the system parameters affect the resonance and antiresonance frequencies of the one lever and two lever LTTSs. One lever LTTS shows low-pass filter type response whereas two lever LTTS can show low pass or band stop filter type response depending on the system parameters. To achieve effective vibration isolation at low frequencies, band gap should be as wide as possible. Moreover, to achieve high level of attenuation within the band gap, imaginary part of the wave vector should be as deep as possible. To achieve wide and deep band gaps, optimization study is performed via genetic algorithm. Prototype of the two lever LTTS having optimized parameters is manufactured. It is shown that analytical and experimental frequency responses are compatible.

ÖZET

ATALET ARTIRIM MEKANİZMALI GERİLİM YAPILARI

Bu tezde, düşük frekanslarda geniş ve derin bant aralıkları elde etmek için atalet artırım mekanizmalarına sahip yeni gerilim yapıları tasarlanmıştır. Birim hücrelerinde bir kaldıraç veya iki kaldıraç bulunan iki farklı kaldıraç tipi gerilim yapısı (LTTS) tanıtılmıştır. Bu iki tip LTTS'nin analitik modelleri elde edilmiştir. Bu birim hücrelerinin titreşim yalıtım performansı belirlenmiştir ve bu birim hücreleri kullanan tek boyutlu periyodik sistemlerin bant yapısı ile karşılaştırılmıştır. Sistem parametrelerinin tek kaldıraçlı ve iki kaldıraçlı LTTS'lerdeki rezonans ve antirezonans frekanslarını nasıl etkilediğini görmek için parametrik çalışmalar yürütülmüştür. Tek kaldıraçlı LTTS, düşük frekansları geçiren filtre tipi tepki gösterirken, iki kaldıraçlı LTTS, sistem parametrelerine bağlı olarak düşük frekansları geçiren veya bant durduran filtre tipi tepki gösterebilir. Düşük frekanslarda etkili titreşim yalıtımı elde etmek için bant aralığı mümkün olduğunca geniş olmalıdır. Ayrıca, bant aralığında titreşim seviyesini yüksek düzeyde azaltmak için dalga vektörünün sanal kısmı mümkün olduğunca derin olmalıdır. Geniş ve derin bant aralıklarına ulaşmak için genetik algoritma ile eniyileme çalışması yapılmıştır. Eniyilenmiş parametrelere sahip iki kaldıraçlı LTTS'nin prototipi üretilmiştir. Analitik ve deneysel frekans tepkilerinin uyumlu olduğu gösterilmiştir.

TABLE OF CONTENTS

LIST OF FIGURES

LIST OF SYMBOLS

BD	Band depth of band-stop filter type two lever LTTS
BW	Bandwidth of band-stop filter type two lever LTTS
k	Spring constant of one lever LTTS
k_1	First spring constant of two lever LTTS
k_2	Second spring constant of two lever LTTS
k_{end}	Stiffness of spring connected between prototype and test fixture
k_t	Total stiffness of band-stop filter type two lever LTTS
l_1	Length of lever in one lever LTTS
l_{11}	Length of first lever in two lever LTTS
l_{12}	Length between two hinges of the first lever in two lever LTTS
l_2	Length between two hinges of the lever in one lever LTTS
l_{21}	Length of second lever in two lever LTTS
l_{22}	Length between two hinges of the second lever in two lever LTTS
m	Mass of the rigid beams of one and two lever LTTS
m_i	Lever mass in one lever LTTS
m_{i1}	First lever mass in two lever LTTS
m_{i2}	Second lever mass in two lever LTTS
m_t	Total mass of band-stop filter type two lever LTTS

α	Amplification ratio of one lever LTTS
α_1	First amplification ratio of two lever LTTS
α_2	Second amplification ratio of two lever LTTS
β	Rotation angle of lever in one lever LTTS
γ	Wave number of one and two lever LTTSs
ω	Excitation frequency

ω_l	Lower limit of the band gap in band-stop filter type two lever LTTS
ω_p	Resonance frequency of one lever LTTS
ω_{p1}	First resonance frequency of two lever LTTS
ω_{p2}	Second resonance frequency of two lever LTTS
ω_u	Upper limit of the band gap in band-stop filter type two lever LTTS
ω_z	Antiresonance frequency of one lever LTTS
ω_{z1}	First antiresonance frequency of two lever LTTS
ω_{z2}	Second antiresonance frequency of two lever LTTS

LIST OF ACRONYMS/ABBREVIATIONS

1D	One Dimensional
2D	Two Dimensional
3D	Three Dimensional
DVA	Dynamic Vibration Absorber
SDOF	Single Degree of Freedom
LTTS	Lever Type Tensegrity Structure

1. INTRODUCTION

This thesis is about applying inertial amplification method that is used for phononic band gap generation to tensegrity structures. Initially, three widely used methods for phononic band gap generation namely Bragg scattering [1-4], local resonance [5-9] and inertial amplification [10-19] are compared according to obtaining large bandgaps at desired frequency ranges.

Phononic band gaps, also known as band gaps for elastic waves, are regions of frequency where wave propagation is prevented in periodic media. They have attracted significant attention in recent years due to their potential for use in a variety of applications such as sound insulation [20-23], vibration control [24-30], and energy harvesting [31,32]. Several methods have been proposed for creating phononic band gaps in periodic media, including Bragg scattering, local resonance and inertial amplification.

Bragg scattering is a method that utilizes the periodicity of the structure to scatter waves at certain frequencies, known as Bragg frequencies. The scattered waves interfere destructively, resulting in a band gap at the Bragg frequency. This method is based on the constructive and destructive interference of waves scattered by a periodic array of scatterers. The lowest frequency gap due to Bragg scattering is of the order of the wave speed (longitudinal or transverse) of the medium divided by the lattice constant [33-35]. Therefore, low wave speeds or large lattice constants are needed to get low frequency Bragg gap. In this method, heavy, low stiffness and large sized structures are required, which is not practical and desired.

Local resonance is a method that utilizes the resonant behavior of a periodic structure to create a band gap. In this method, the resonance of the structure is tuned to a specific frequency, resulting in a band gap at that frequency. This method is based on the enhancement of the natural frequency of the structure by introducing resonant elements. Band gaps can be obtained at frequencies lower than Bragg Scattering via using local resonators [8], [34-39]. But, heavy resonators are required in order to acquire large gaps at low frequencies.

Inertial amplification is a method that utilizes inertial amplification mechanisms to increase the effective inertia of the unit cell. Hence, the dynamic mass of a structure when subject to excitations can be much larger than its static mass. Due to increased effective inertia, band gaps at low frequencies can be obtained [40-44]. The inertial amplification method solves deficiencies of the previous methods. Thus, wide band gaps at low frequencies are obtained.

Inertial amplification method has been applied to 1D, 2D and 3D periodic solid structures [45-47]. This study focuses on the use of inertial amplification for creating phononic band gaps in tensegrity structures. Tensegrity structures, which are composed of a combination of tensile and compressive elements, have gained significant attention in recent years due to their unique mechanical properties and potential for use in a variety of applications such as architectural [48-50], aerospace [51,52], and mechanical engineering [48], [53,54]. The combination of tensile and compressive elements in these structures results in a lightweight design. The tensile elements can only carry tensile load as they can be in the form of wire rope, string or chain. One of the challenges with these structures is their relatively low stiffness and strength when compared to traditional structures made of elements that can support both tension, compression and bending loads. By utilizing inertial amplification to create phononic band gaps in tensegrity structures, it is expected that the low frequency excitations can be mitigated with the use of lightweight elements. The study focuses on the design, analysis, and experimentation of tensegrity structures utilizing inertial amplification, with the goal of developing a new design approach for tensegrity structures. This work includes the development of design guidelines for incorporating inertial amplifiers into tensegrity structures, the numerical analysis of the dynamic response of tensegrity structures with inertial amplifiers, and the experimentation of tensegrity structures with inertial amplifiers. The main outcome of this research is the development of a new design approach for tensegrity structures that utilizes inertial amplification, which results in structures with improved vibration characteristics. This study provides potential applications in various fields such as architecture, aerospace and mechanical engineering.

1.1. Literature Review

This research is about using inertial amplification method on tensegrity structures. Firstly, inertial amplification method will be explained.

The effects of inertial amplification can be shown via comparison between results of inertial amplification and well-known Dynamic Vibration Absorber (DVA) [55-59]. In [55], SDOF systems equipped with DVA and different lever types of inertial amplification mechanisms are used for vibration isolation [55].

According to [55], there are two types of lever type anti-resonant vibration isolators such as Type 1 and Type 2 based on the location of pivot point according to load and isolator mass. For Type 1 isolator, the location of pivot point connected to base is between load and isolator. On the other hand, for Type 2 isolator, the location of pivot point connected to load is between base and isolator [55]. In other words, the isolator mass movement is greater in Type 2 than in Type 1 with same load mass movement. However, in both cases, effective inertia of the isolator mass is amplified due to the lever.

Bandwidth values of these three models are different from each other. As explained in [55], when a low frequency isolation is sought after with small mass, bandwidth of a Type 2 isolator can be approximately 4 times that of a Type 1 isolator and approximately 16 times that of a DVA, with the same parameters. Hence, lever type inertially amplified vibration isolators offer a much better performance compared to DVA at low frequencies.

In order to create a phononic bandgap in a periodic structure, there are two widely known methods which are Bragg scattering [1-4] and local resonance [5-9], [40]. Inertial amplification method [10-19] is a new alternative method in this field. The advantages of inertial amplification method as against the other two methods are indicated in [17], [40,41], [60,61].

In [40,41], bridge type amplification mechanisms are used instead of lever type amplification mechanisms (Type 1 and Type 2 in [55]). Nevertheless, all these designs utilize the concept of inertial amplification to achieve low frequency vibration isolation.

Comparison between Bragg Scattering, Local Resonance and Inertial Amplification is performed in [41]. Both of Local Resonance and Inertial Amplification have deep antiresonance notches but they are different according to energy localization. In local resonance model, energy is transmitted through the structure but energy is localized at the excitation source and does not propagate for the inertial amplification model [41].

Both of Bragg Scattering and Inertial Amplification are similar in terms of energy localization [41]. For both models, transmitted energy is decreased from input location to output location but decrease rate in inertial amplification model is much more than the Bragg scattering model. Moreover, depth of the band gaps in frequency response function plots are qualitatively different [41]. Due to inertial coupling in the inertially amplified model, antiresonance notch appears, which provides high level of attenuation. On the other hand, no such antiresonance effect occurs in the Bragg scattering model.

Tensegrity structure is a type of structural system that integrates tension and compression elements to create a stable and rigid form. This concept was introduced by Buckminster Fuller in the 1940s and has since been developed by researchers in various fields such as architecture [48-50], engineering [48], [53,54] and robotics [62-68]. The combination of tension elements such as cables or strings and compression elements such as struts or columns results in a structure that is both strong and efficient. The tension elements prevent the structure from collapsing while the compression elements resist compression and prevent buckling, resulting in the forces being evenly distributed throughout the structure leading to its lightweight and efficient design.

Tensegrity structures are popular in architecture for their strength and stability, with examples such as domes and bridges. They are able to distribute forces evenly throughout the structure, making them suitable for use in harsh conditions and heavy loads. Tension elements provide stability while compression elements provide rigidity. These structures are also known for their efficiency, as the tension elements are lightweight and require less material and energy to construct, making them a sustainable and environmentally friendly option for construction [69].

Tensegrity structures are also popular for their aesthetic appeal [70,71]. The combination of tension and compression elements creates a visually dynamic structure, with the compression elements appearing to float and the tension elements that support them can be quite thin and almost invisible. This creates a memorable and visually stunning structure that can serve as a landmark for a community.

However, designing and constructing tensegrity structures comes with some challenges. Ensuring the structure is stable and rigid is important as a small change in the position of one element can undermine its stability. Additionally, ensuring the balance between tension and compression elements is crucial as an imbalance can result in collapsing or buckling of the structure. Careful consideration and advanced computer simulations may be necessary to ensure the stability of the structure. Despite these challenges, tensegrity structures offer many advantages in architecture, making them a popular choice for those looking to create strong, efficient, and sustainable structures.

Tensegrity structures are a topic of interest in the field of robotics due to their potential for use in the design of soft robots and bio-inspired robots [67]. Tensegrity robot structures can be used for space industry, for instance, The ReCTeR is utilized for NASA space mission. Soft robots are made of flexible materials, such as silicone or elastomers, and are designed to adapt to their environment and conform to objects in their path. Tensegrity structures are ideal for use in the design of soft robots as they provide support and stability while allowing for flexibility and adaptability. Research has demonstrated the potential benefits of using tensegrity structures in soft robots. For example, tensegrity structures can enhance the stability and robustness of soft robots, making them better suited for use in challenging environments. Additionally, tensegrity structures can increase the efficiency of soft robots, allowing them to perform tasks with greater ease and speed. Furthermore, tensegrity structure embedded torsional movement mechanisms can be used in robotics [72,73].

Tensegrity structures are present in biological systems [74-78] such as cells and bones, where they provide stability, rigidity and distribute forces evenly. The structure is created by the arrangement of tension and compression elements, such as actin filaments, microtubules, collagen fibers and mineralized hydroxyapatite, in a manner that creates a balance between stability and adaptability. Studies have shown that the mechanical properties of cells and tissues, including stiffness and elasticity, are influenced by the arrangement of tensegrity elements [79]. Microtubules and actin filaments of multicellular organism cell are represented by struts and pre-stretched cables of tensegrity structure respectively.

In the design of bio-inspired robots, tensegrity structures mimic the mechanical properties of biological systems, including strength, stability, and flexibility. This makes them an ideal choice for engineers and scientists working in the field of robotics who are looking to create robots that are inspired by biological systems [80].

Tensegrity structure embedded torsional movement mechanisms [81-83] are used in [84, 85] for vibration isolation, in [86-89] for airplane wing design.

For vibration isolation, 1D axial to rotary motion conversion mechanism which provides large rotational motion as a result of small axial movement is used in [84]. In this model, axial and torsional stiffnesses are not high and effective mass is amplified via large rotational movement, which provides a band gap at low frequencies [84].

1.2. Motivation and Research

Earlier studies show that inertial amplification method offers wider antiresonance notch compared to dynamic vibration absorbers [55]. Moreover, when lattice structures are investigated, inertial amplification provides wider band gap than the Bragg Scattering, Local Resonance methods [40,41]. Hence, inertial amplification method has a great potential in vibration isolation.

Tensegrity structures have a wide range of usage including architecture and robotics. They include tension and compression elements such as cables and strings; struts and columns, respectively. Tension elements are generally lightweight so that the overall tensegrity structure can be lightweight.

In this thesis, inertial amplification is used on a tensegrity structure. Inertial amplification and tensegrity structure are two different topics and intersection of these is not common in the literature. There are some studies that exploit torsional motion of tensegrity structures to isolate longitudinal excitations [84-86]. In this thesis, a novel design will be introduced that does not rely on torsional motion.

Tensegrity structures, with their lightweight and compact design, are cost-effective and easy to manufacture. This gives tensegrity structures with embedded inertial amplification mechanisms an advantage over existing inertial amplification structures in the literature. Moreover, the fact that an inertial amplification structure operating under tension has not yet been designed opens up new potential applications, such as tension systems that do not transmit vibrations.

The main motivation for doing this research is creating a novel tensegrity structure design that has embedded inertial amplification mechanisms to isolate vibrations in a wide frequency range.

This research includes four chapters which are introduction, analytical studies, experimental validation and conclusion. Firstly, brief information including definitions, literature review, motivation and outline of research is given in the introduction part. The second part is about analytical model that contains explanation of analytical equations and graphs, optimization of the analytical model to have a large frequency range of operation. The third part is about experimentation which includes prototyping stage and experimental results. Conclusion is fourth part of thesis, that includes the results of this thesis.

2. ANALYTICAL STUDIES

The core model of this thesis is a tensegrity structure with embedded inertial amplification mechanisms. Lever type inertial amplification mechanisms are used in the structure, so it is named as Lever Type Tensegrity Structure (LTTS). LTTS includes lever type beams, springs and tension elements. There are two types of LTTS in this research, which contain one or two levers in a unit cell.

One lever LTTS involves two rigid beams of mass m that can only translate horizontally, one rigid lever of mass m_i that can translate horizontally and rotate, two inextensible cables and one spring with stiffness k. The model is shown in Figure 2.1

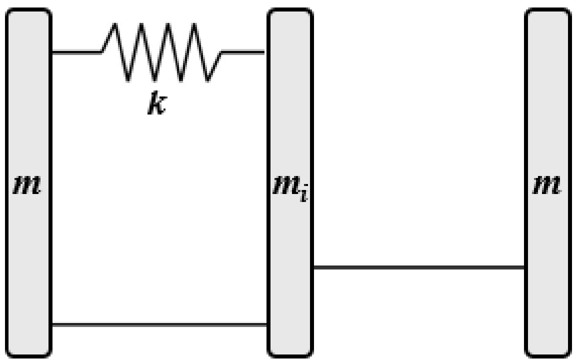

Figure 2.1. One lever LTTS.

When the masses m are moved away from one another, the rigid lever with mass m_i rotates (see in Figure 2.2(a)). Due to the presence of the spring, the masses can return to their original state when released. The relative motion (u_{i+1}-u_i) of the masses m, creates rotation (β) for the lever with mass m_i. Assuming that l_2 is small compared to l_1 in Figure 2.2(b), large amount of rotation can be obtained from small relative motion between the masses m. In order to quantify the amplification in the system, lever ratio (α) is used:

$$\alpha = \frac{l_1}{l_2}. \tag{2.1}$$

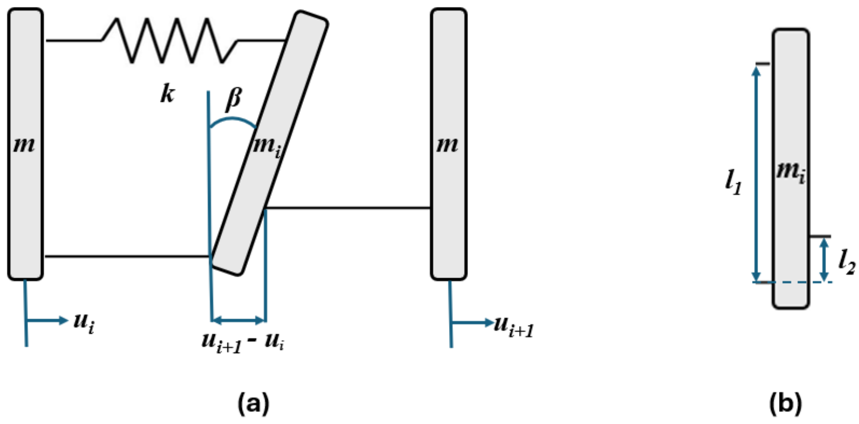

Figure 2.2. (a) Detailed movement of one lever LTTS (b) Dimensions of the lever.

To find the equation of motion of the structure, Lagrange's method will be used. The Lagrangian (L) is equal to the difference between kinetic energy (T) and potential energy (V):

$$L = T - V. \tag{2.2}$$

Total kinetic energy includes translational kinetic energy of two beams at the ends and translational and rotational kinetic energy of the lever in the middle, which are shown below:

$$T = T_{1tra} + T_{3tra} + T_{2tra} + T_{2rot}, \tag{2.3}$$

$$T_{1tra} = \frac{1}{2} m (\dot{u}_i)^2, \tag{2.4}$$

$$T_{3tra} = \frac{1}{2} m (\dot{u}_{i+1})^2, \tag{2.5}$$

$$T_{2tra} = \frac{1}{2} m_i \left(\dot{u}_i + \frac{(\dot{u}_{i+1} - \dot{u}_i)\alpha}{2} \right)^2, \tag{2.6}$$

$$T_{2rot} = \frac{1}{24} m_i \big(\alpha(\dot{u}_{i+1} - \dot{u}_i)\big)^2. \tag{2.7}$$

Total potential energy contains only the potential energy of the spring. Due to the arrangement of the cables, input displacements are amplified by $\alpha = l_1/l_2$:

$$V = \frac{1}{2}k\alpha^2(u_{i+1} - u_i)^2. \tag{2.8}$$

The Lagrangian (L) is shown below according to total kinetic (Equation (2.3)) and potential (Equation (2.8)) energies:

$$\begin{aligned} L = \frac{1}{2}m((\dot{u}_i)^2 + (\dot{u}_{i+1})^2) + \frac{1}{2}m_i(\dot{u}_i)^2 + \frac{1}{6}m_i\alpha^2(\dot{u}_{i+1} - \dot{u}_i)^2 \\ + \frac{1}{2}m_i\alpha\big(\dot{u}_i(\dot{u}_{i+1} - \dot{u}_i)\big) - \frac{1}{2}k\alpha^2(u_{i+1} - u_i)^2. \end{aligned} \tag{2.9}$$

Equation of motion for this model is obtained by

$$\frac{d}{dt}\left(\frac{\partial L}{\partial \dot{u}_{i+1}}\right) - \frac{\partial L}{\partial u_{i+1}} = 0, \tag{2.10}$$

$$\left(m + \frac{m_i\alpha^2}{3}\right)\ddot{u}_{i+1} + \left(\frac{m_i\alpha}{2} - \frac{m_i\alpha^2}{3}\right)\ddot{u}_i + k\alpha^2 u_{i+1} - k\alpha^2 u_i = 0. \tag{2.11}$$

The term that multiplies the second derivative of output displacement ($\ddot{u}_{i+1}$) is the effective mass of one lever LTTS. Effective mass can be more than m+m_i, if α is more than 1.732, which indicates the presence of inertial amplification.

According to Equation (2.11), the resonance (ω_p) and antiresonance (ω_z) frequencies can be obtained as

$$\omega_p = \sqrt{\frac{k\alpha^2}{m + \frac{m_i\alpha^2}{3}}}, \tag{2.12}$$

$$\omega_z = \sqrt{\frac{k\alpha^2}{\frac{m_i\alpha^2}{3} - \frac{m_i\alpha}{2}}}. \tag{2.13}$$

Considering the antiresonance frequency equation (Equation (2.13)), the denominator can be equal zero at α=1.5, implying that the antiresonance frequency approaches infinity, i.e., there is no antiresonance frequency.

Transmissibility ($TR(\omega)$) can be calculated as

$$TR(\omega) = \left|\frac{1 - \left(\frac{\omega}{\omega_z}\right)^2}{1 - \left(\frac{\omega}{\omega_p}\right)^2}\right|, \tag{2.14}$$

$$TR(\omega) = \left|\frac{k\alpha^2 + \omega^2\left(\frac{m_i\alpha}{2} - \frac{m_i\alpha^2}{3}\right)}{k\alpha^2 - \omega^2\left(m + \frac{m_i\alpha^2}{3}\right)}\right|. \tag{2.15}$$

Transmissibility ($TR(\infty)$) at large frequencies ($\omega \gg \omega_p, \omega_z$) can be found as

$$TR(\infty) = \left|\frac{\frac{m_i\alpha^2}{3} - \frac{m_i\alpha}{2}}{m + \frac{m_i\alpha^2}{3}}\right|. \tag{2.16}$$

For k=4 N/m, m=1kg, m_i=1kg and α=4, transmissibility graph is shown in Figure 2.3.

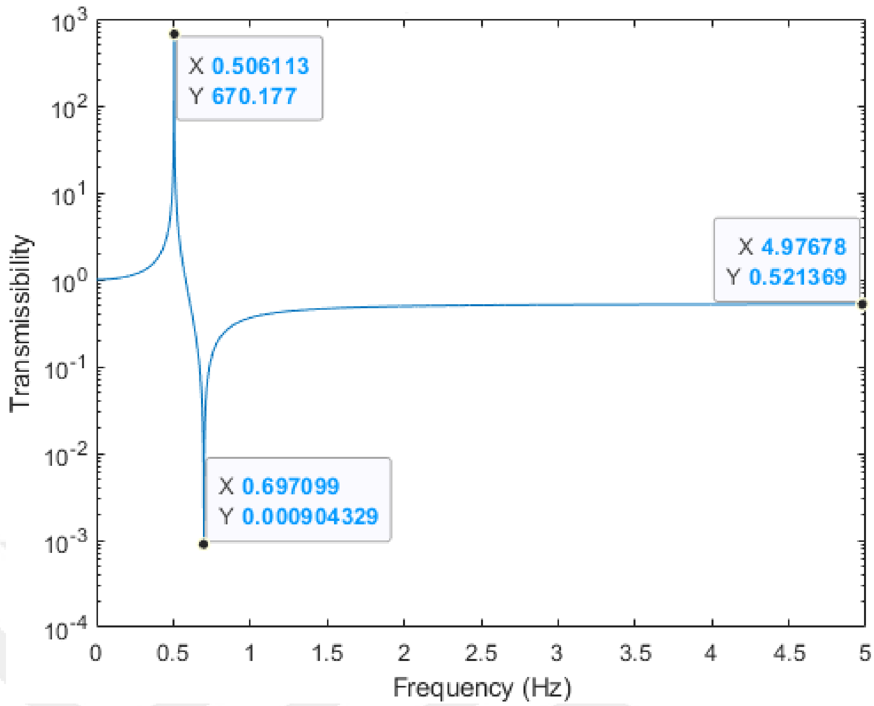

Figure 2.3. Transmissibility graph of one lever LTTS for k=4 N/m, m=1kg, m_i=1kg and α=4.

Resonance frequency (ω_p) and antiresonance frequency (ω_z) are at 0.506 Hz and 0.697 Hz, respectively and these values agree with Equations (2.12) and (2.13), respectively. Transmissibility ($TR(\infty)$) at large frequencies ($\omega >> \omega_p$, ω_z) is calculated as 0.52 according to Equation (2.16), which also agrees with the graph in Figure 2.3.

For the one lever LTTS, antiresonance frequency (ω_z) is always higher than resonance frequency (ω_p) because the denominator of antiresonance frequency equation (Equation (2.13)) is always less than the denominator of resonance frequency equation (Equation (2.12)) while the numerators of both equations are the same.

The parameters (m, m_i, k, α) affect the frequency response of the system. To examine the effect of these parameters, parametric study for each one is performed.

First of all, one lever LTTSs having different spring constants (k=2N/m, 4N/m and 8N/m) are compared. Spring constant does not change transmissibility at large frequencies

($\omega >> \omega_p$, ω_z) as indicated in Figure 2.4, since the equation of the transmissibility at large frequencies (Equation (2.16)) does not include the k term. However, antiresonance (ω_z) and resonance (ω_p) frequencies increase as the spring constant (k) increases (see Figure 2.4).

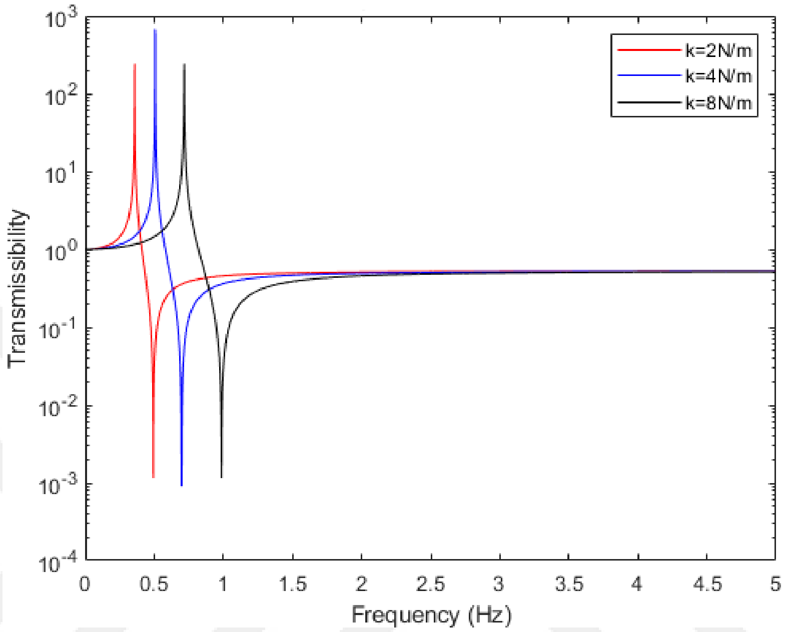

Figure 2.4. Transmissibility graph of one lever LTTS (m=1kg, m_i=1kg, α=4) for k=2 N/m, 4 N/m and 8 N/m.

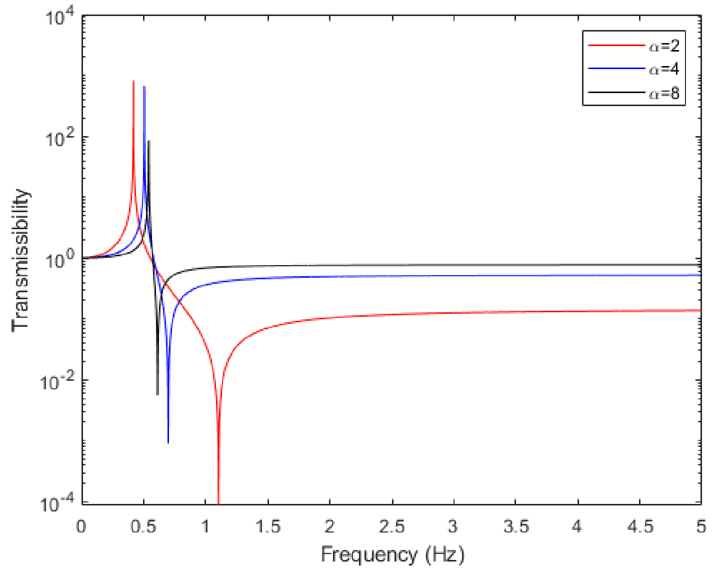

Figure 2.5. Transmissibility graph of one lever LTTS (k=4 N/m, m=1kg, m_i=1kg) for α=2, 4 and 8.

Secondly, one lever LTTSs having different α values (α=2, 4 and 8) are compared. As α increases, transmissibility at large frequencies ($\omega >> \omega_p$, ω_z) increases, which is shown in Figure 2.5. The effect of α on antiresonance and resonance frequencies are not the same. An increase in α rises resonance frequency but decreases antiresonance frequency as seen in Figure 2.5.

When α = 1.5, antiresonance frequency of the one lever LTTS approaches infinity. In order to see the effect of varying α close to 1.5, Figure 2.6 can be investigated. Notice that, when α is less than 1.5, there is no antiresonance frequency. However, α is larger than 1.5 results in an antiresonance frequency. Moreover, when α decreases, resonance frequency of the system decreases, as well.

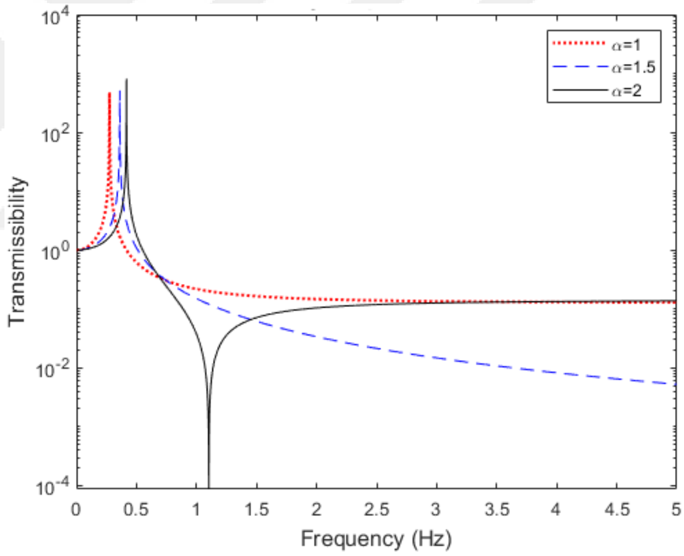

Figure 2.6. Transmissibility graph of one lever LTTS (k=4 N/m, m=1kg, m_i=1kg) for α=1, 1.5 and 2.

Then, one lever LTTSs having different m values (m=1kg, 3kg and 10kg) are compared. m does not change antiresonance frequency as indicated in Figure 2.7, since the equation of the antiresonance frequency (Equation (2.13)) does not include m term. However, resonance frequency increases as m increases, which is demonstrated in Figure 2.7. m has inverse proportion with transmissibility at large frequencies, i.e., increasing m decreases transmissibility as seen in Figure 2.7.

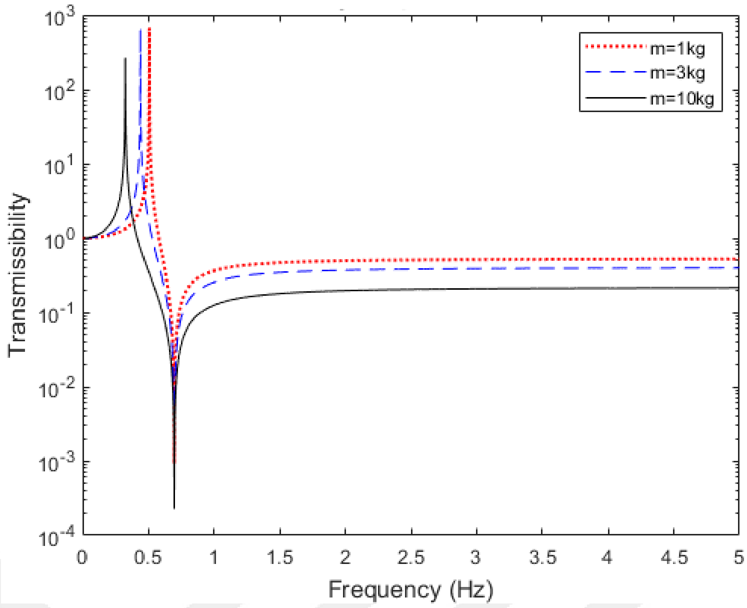

Figure 2.7. Transmissibility graph of one lever LTTS (k=4 N/m, m_i=1kg, α=4) for m=1kg, 3kg and 10kg.

Lastly, one lever LTTSs having different m_i values (m_i=0.1kg, 0.3kg and 1kg) are compared. Increasing the lever mass m_i decreases both antiresonance and resonance frequencies. Moreover, this also increases transmissibility at large frequencies as depicted in Figure 2.8.

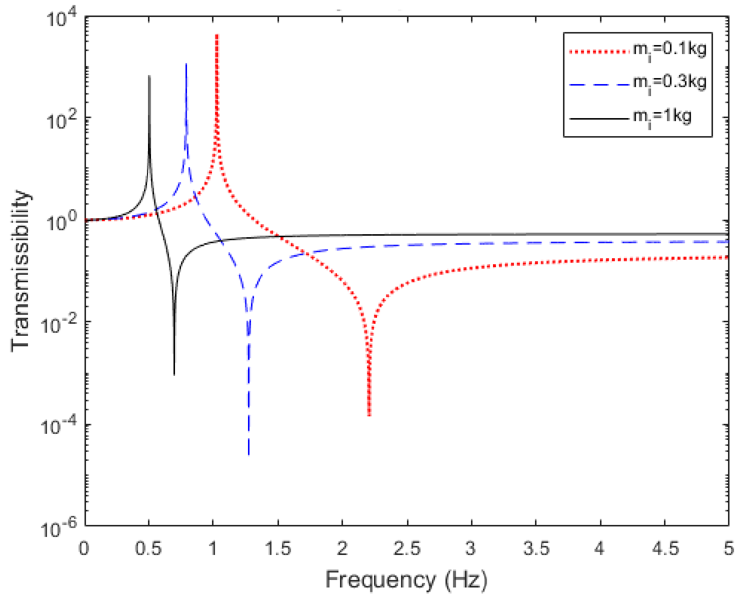

Figure 2.8. Transmissibility graph of one lever LTTS (k=4 N/m, m=1kg, α=4) for m_i=0.1kg, 0.3kg and 1kg.

For vibration isolation, a 1D periodic tensegrity structure that has a unit cell as the one lever LTTS is generated. The periodic structure can be seen in Figure 2.9(a) whereas the unit cell is depicted in Figure 2.9(b).

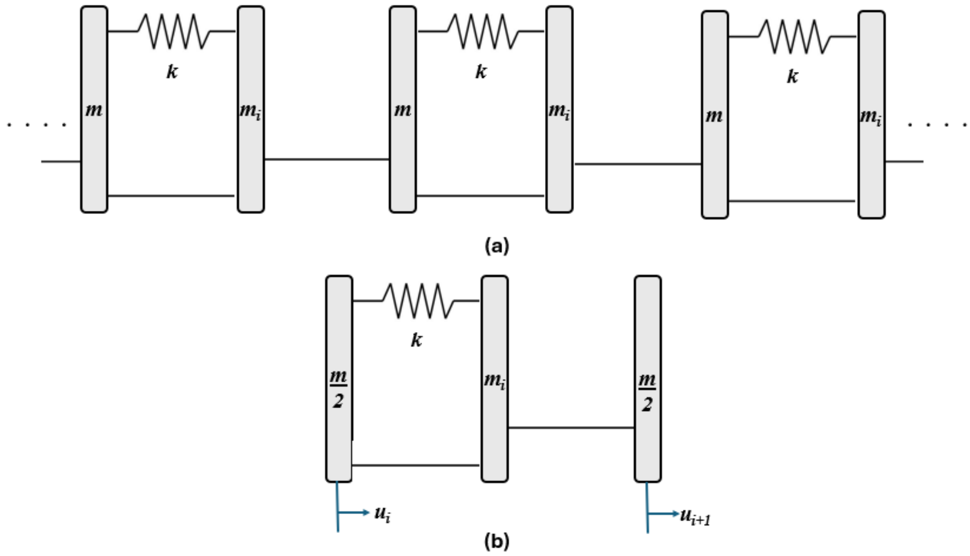

Figure 2.9. (a) 1D periodic model of one lever LTTS (b) One lever LTTS unit cell.

Equations of motion for the unit cell of one lever LTTS are expressed as

$$\mathrm{M}_{11}\ddot{u}_i + \mathrm{M}_{12}\ddot{u}_{i+1} + \hat{k}u_i - \hat{k}u_{i+1} = 0, \tag{2.17}$$

$$\mathrm{M}_{21}\ddot{u}_i + \mathrm{M}_{22}\ddot{u}_{i+1} - \hat{k}u_i + \hat{k}u_{i+1} = 0, \tag{2.18}$$

$$\mathrm{M}_{11} = 0.5m + m_i - m_i\alpha + \frac{m_i\alpha^2}{3}, \tag{2.19}$$

$$\mathrm{M}_{12} = \mathrm{M}_{21} = \frac{m_i\alpha}{2} - \frac{m_i\alpha^2}{3}, \tag{2.20}$$

$$\mathrm{M}_{22} = 0.5m + \frac{m_i\alpha^2}{3}, \tag{2.21}$$

$$\hat{k} = k\alpha^2. \tag{2.22}$$

Equations of motion can be written in matrix form by defining mass matrix **M**, stiffness matrix **K**, displacement vector **u** and acceleration vector **ü**:

$$\mathbf{M}\ddot{\mathbf{u}} + \mathbf{K}\mathbf{u} = \mathbf{0}, \tag{2.23}$$

$$\mathbf{M} = \begin{bmatrix} \mathrm{M}_{11} & \mathrm{M}_{12} \\ \mathrm{M}_{21} & \mathrm{M}_{22} \end{bmatrix}, \tag{2.24}$$

$$\mathbf{K} = \begin{bmatrix} \hat{k} & -\hat{k} \\ -\hat{k} & \hat{k} \end{bmatrix}, \tag{2.25}$$

$$\ddot{\mathbf{u}} = \begin{bmatrix} \ddot{u}_i \\ \ddot{u}_{i+1} \end{bmatrix}, \tag{2.26}$$

$$\mathbf{u} = \begin{bmatrix} u_i \\ u_{i+1} \end{bmatrix}. \tag{2.27}$$

In order to obtain the equation of motion of the infinitely periodic structure, Bloch's Theorem can be used:

$$u_{i+1} = e^{j\gamma} u_i. \tag{2.28}$$

Displacement vector **u** transforms displacement of the nodes in the Bloch reduced coordinate $\tilde{u}$ via the transformation matrix **T**:

$$\tilde{u} = u_i, \tag{2.29}$$

$$\mathbf{u} = \mathbf{T}\tilde{u}, \tag{2.30}$$

$$\mathbf{T} = \begin{bmatrix} 1 \\ e^{j\gamma} \end{bmatrix}. \tag{2.31}$$

To obtain the dispersion curve, Bloch transformation can be applied. Moreover, dynamic stiffness matrix **D** is obtained as

$$\mathbf{D} \equiv \mathbf{K} - \omega^2 \mathbf{M}, \tag{2.32}$$

$$\mathbf{D} = \begin{bmatrix} \hat{k} - \omega^2 \mathrm{M}_{11} & -\hat{k} - \omega^2 \mathrm{M}_{12} \\ -\hat{k} - \omega^2 \mathrm{M}_{21} & \hat{k} - \omega^2 \mathrm{M}_{22} \end{bmatrix}. \tag{2.33}$$

Transformed dynamic stiffness matrix $\widetilde{\mathbf{D}}$ is acquired by multiplying $\mathbf{T}^{\mathrm{H}}$ (Hermitian transpose of transformation matrix), **D** and **T**:

$$\widetilde{\mathbf{D}} = \mathbf{T}^{\mathrm{H}} \mathbf{D} \mathbf{T}, \tag{2.34}$$

$$\widetilde{\mathbf{D}} = \begin{bmatrix} 1 & e^{-j\gamma} \end{bmatrix} \begin{bmatrix} \hat{k} - \omega^2 \mathrm{M}_{11} & -\hat{k} - \omega^2 \mathrm{M}_{12} \\ -\hat{k} - \omega^2 \mathrm{M}_{21} & \hat{k} - \omega^2 \mathrm{M}_{22} \end{bmatrix} \begin{bmatrix} 1 \\ e^{j\gamma} \end{bmatrix}, \tag{2.35}$$

$$\widetilde{\mathbf{D}} = 2\hat{k} - \omega^2 (\mathrm{M}_{11} + \mathrm{M}_{22}) - \left(\hat{k} + \omega^2 \mathrm{M}_{12}\right)\left(e^{j\gamma} + e^{-j\gamma}\right). \tag{2.36}$$

Exponential terms are eliminated and converted to trigonometric terms by using Euler's identity:

$$e^{j\gamma} = \cos\gamma + j\sin\gamma\,, \tag{2.37}$$

$$e^{-j\gamma} = \cos\gamma - j\sin\gamma\,, \tag{2.38}$$

$$\widetilde{\mathbf{D}}(\gamma, \omega)\tilde{u} = 0. \tag{2.39}$$

The equation that is obtained from Bloch Transformation becomes an eigenvalue problem for a harmonic free wave motion. According to this equation, γ(wave number) can be solved as

$$cos\gamma = \frac{2k\alpha^2 - \omega^2\left(m + m_i - m_i\alpha + \frac{2m_i\alpha^2}{3}\right)}{2k\alpha^2 + \omega^2\left(m_i\alpha - \frac{2m_i\alpha^2}{3}\right)}. \qquad (2.40)$$

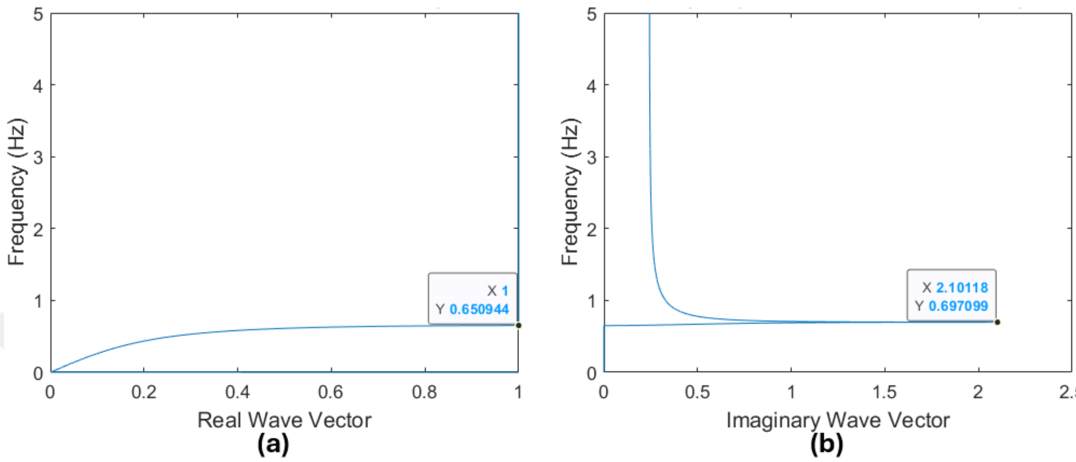

Figure 2.10. Complex band structure of the 1D periodic model generated by unit cell of one lever LTTS for k=4 N/m, m=1kg, m_i=1kg and α=4 (a) Real wave vector (b) Absolute value of imaginary wave vector.

According to Equation (2.40), complex band structure graphs can be obtained. For k=4 N/m, m=1kg, m_i=1kg and α=4, wave vector graphs with respect to frequency (Hz) are obtained, which are indicated in Figure 2.10.

Band gap starting frequency of lattice structure is 0.65 Hz (see Figure 2.10(a)), which is slightly lower than the notch frequency at 0.697 Hz (see Figure 2.10(b)). The notch frequency in Figure 2.10(b) is equal to the antiresonance frequency of the one lever LTTS in Figure 2.3. The notch in the imaginary part of the wave vector is due to the inertial coupling effect. Above the notch frequency, imaginary wave vector value converges to a constant value as frequency goes to infinity, which is shown in Figure 2.10(b). Imaginary part of the wave vector is related to attenuation and higher attenuation signifies a deeper band gap in a finite periodic system. Moreover, to obtain a wide low frequency band gap, band gap starting frequency should be as low as possible.

The parameters (m, m_i, k, α) influence the band gap starting frequency and band depth. To examine their effects, parametric studies are conducted for the periodic structure having one lever LTTS in its unit cell.

First of all, one lever LTTSs having different spring constants (k=2N/m, 4N/m and 8N/m) are compared. Spring constant does not alter band depth of the system which is related to the attenuation level when frequency goes to infinity as indicated in Figure 2.11. However, band gap starting frequency is raised by increasing stiffness value, which is undesirable to obtain a wide band gap at low frequencies.

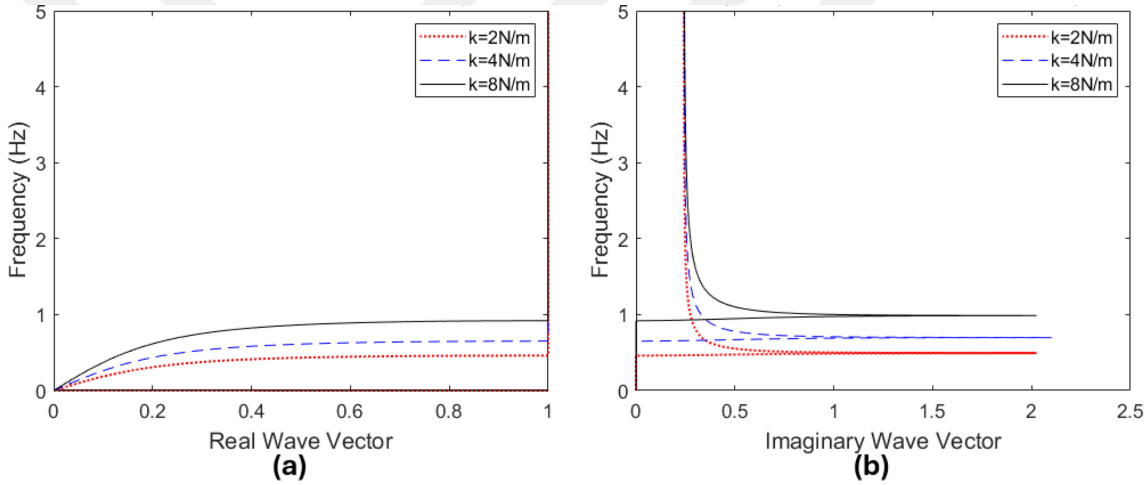

Figure 2.11. Complex band structure of the 1D periodic model generated by unit cell of one lever LTTS (m=1kg, m_i=1kg and α=4) for k=2 N/m, 4 N/m and 8 N/m (a) Real wave vector (b) Absolute value of imaginary wave vector.

Secondly, one lever LTTSs having different α values (α=2, 4 and 8) are compared. When α increases, band gap starting frequency and band depth decrease, which is shown in Figure 2.12. Decrease in band gap starting frequency is desirable but decrease in band depth is not desirable to get a wide and deep band gap at low frequencies resulting in a trade-off.

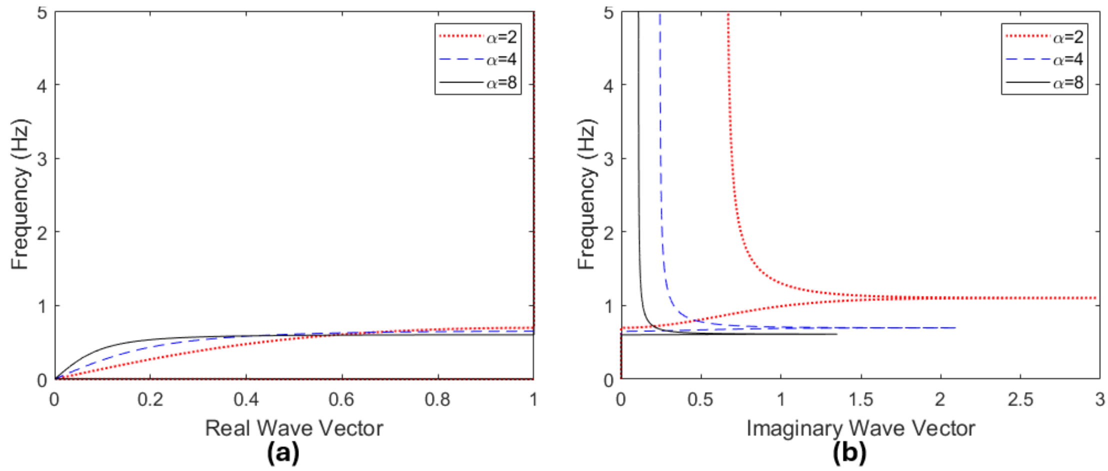

Figure 2.12. Complex band structure of the 1D periodic model generated by unit cell of one lever LTTS (k=4N/m, m=1kg and m_i=1kg) for α=2, 4 and 8 (a) Real wave vector (b) Absolute value of imaginary wave vector.

When α = 1.5, notch frequency of the one lever LTTS approaches infinity. In order to see the effect of varying α close to 1.5, Figure 2.13 can be investigated. Notice that, when α is less than 1.5, there is no notch frequency in the imaginary part of the wave vector. Moreover, when α is smaller than 1.5, band gap starting frequency decreases, as well.

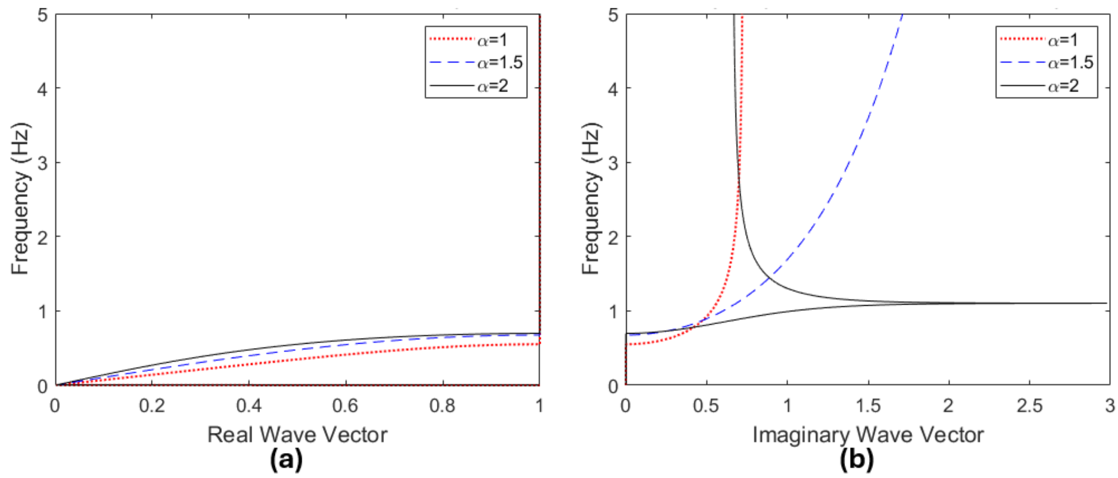

Figure 2.13. Complex band structure of the 1D periodic model generated by unit cell of one lever LTTS (k=4N/m, m=1kg and m_i=1kg) for α=1, 1.5 and 2 (a) Real wave vector (b) Absolute value of imaginary wave vector.

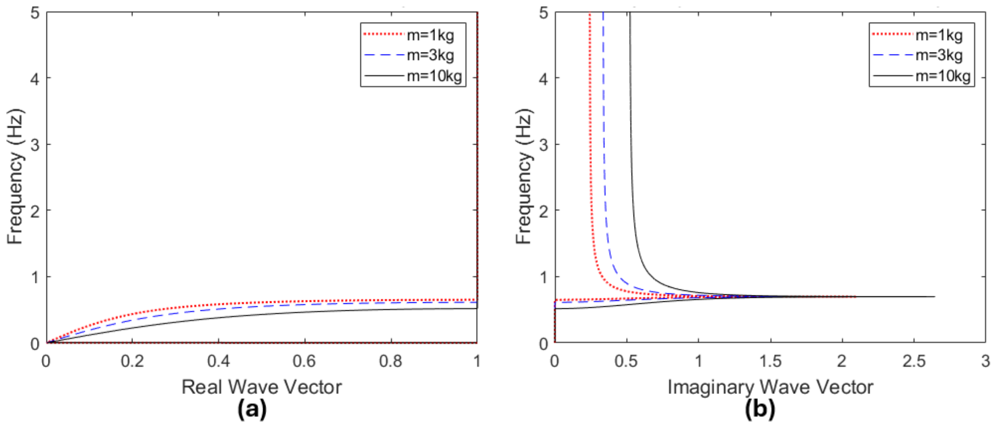

Figure 2.14. Complex band structure of the 1D periodic model generated by unit cell of one lever LTTS (k=4N/m, m_i=1kg and α=4) for m=1kg, 3kg and 10kg (a) Real wave vector (b) Absolute value of imaginary wave vector.

Then, one lever LTTS having different m values (m=1kg, 3kg and 10kg) are compared. m does not alter the notch frequency in the imaginary part of the wave vector as seen in Figure 2.14(b). However, higher attenuation and lower band gap starting frequency are obtained when m is increased.

Lastly, one lever LTTSs having different m_i values (m_i=0.1kg, 0.3kg and 1kg) are compared. An increase in the lever mass m_i decreases band gap starting frequency, which is desirable to obtain a wide low-frequency band gap. However, band depth diminishes by increasing m_i as demonstrated in Figure 2.15(b).

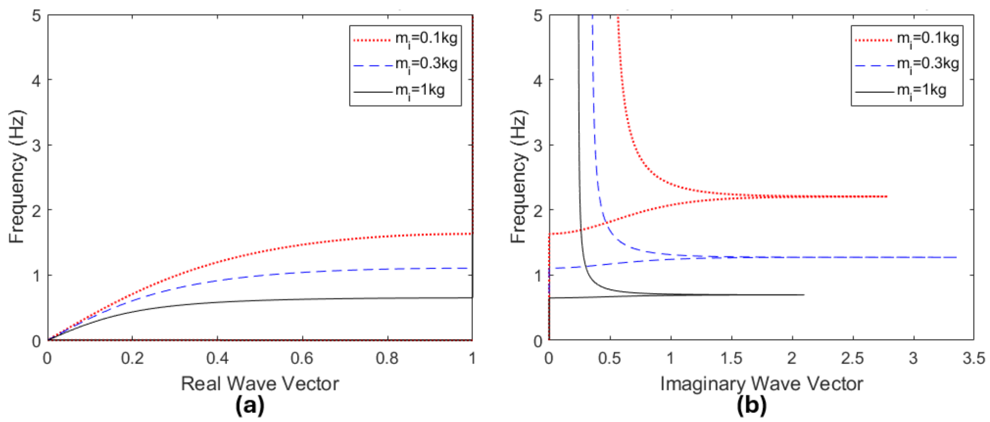

Figure 2.15. Complex band structure of the 1D periodic model generated by unit cell of one lever LTTS (k=4N/m, m=1kg and α=4) for m_i=0.1kg, 0.3kg and 1kg (a) Real wave vector (b) Absolute value of imaginary wave vector.

Two lever LTTS involves two rigid beams of mass *m* that can only translate along the horizontal axis, two rigid levers of mass m_{i1} and m_{i2} that can translate and rotate, three inextensible cables and two springs with stiffnesses k_1 and k_2. The model can be seen in Figure 2.16(a).

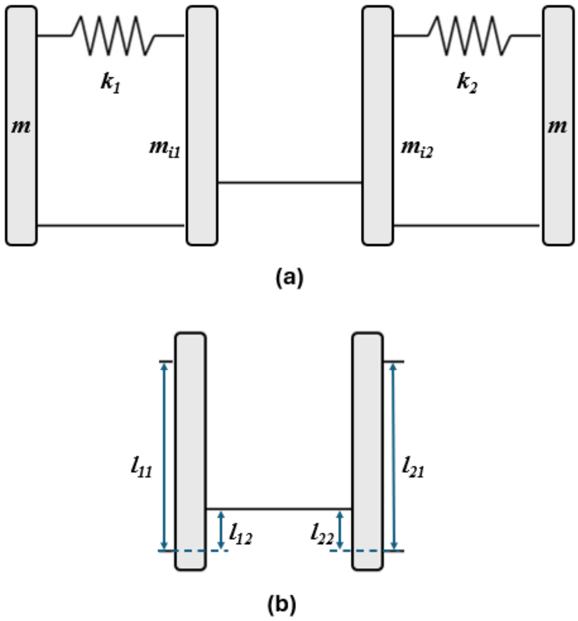

Figure 2.16 (a) Two lever LTTS (b) Lever dimensions.

When the masses *m* are moved away from one another, the rigid levers with masses m_{i1} and m_{i2} rotate (see in Figure 2.17). Due to the presence of the springs, the system can return to its original state when released. The relative motion (u_{i+1}-u_{i-1}) of the masses *m*, creates rotation for the levers with masses m_{i1} and m_{i2}. Assuming that l_{12} and l_{22} are small compared to l_{11} and l_{21} respectively, which are shown in Figure 2.16(b), a large amount of rotation can be obtained from small relative motion between the masses *m*. In order to quantify the amplification in the system, lever ratios (α_1 and α_2) are used:

$$\alpha_1 = \frac{l_{11}}{l_{12}}, \tag{2.41}$$

$$\alpha_2 = \frac{l_{21}}{l_{22}}. \tag{2.42}$$

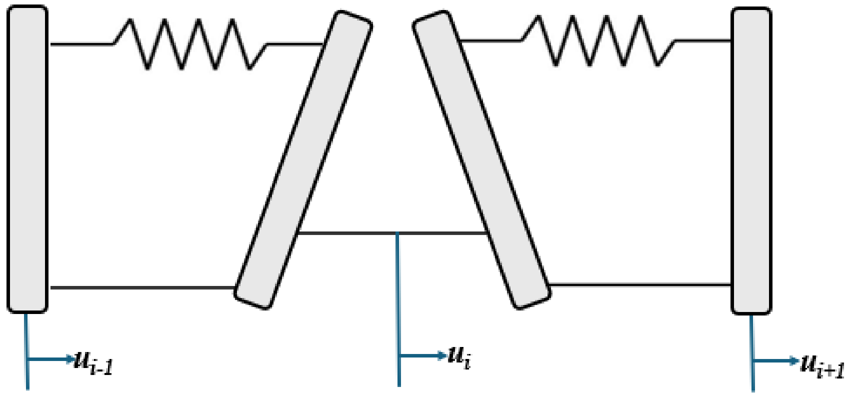

Figure 2.17 Detailed movement of two lever LTTS.

Equations of motion for the two lever LTTS are shown below:

$$\bar{M}_{11}\ddot{u}_i + \bar{M}_{12}\ddot{u}_{i+1} + \left(\hat{k}_1 + \hat{k}_2\right)u_i - \hat{k}_2 u_{i+1} = \bar{m}_i\ddot{u}_{i-1} + \hat{k}_1 u_{i-1}, \tag{2.43}$$

$$\bar{M}_{11}\ddot{u}_i + \bar{M}_{22}\ddot{u}_{i+1} - \hat{k}_2 u_i + \hat{k}_2 u_{i+1} = 0, \tag{2.44}$$

$$\bar{M}_{11} = \frac{m_{i1}{\alpha_1}^2}{3} + \frac{m_{i2}{\alpha_2}^2}{3}, \tag{2.45}$$

$$\bar{M}_{12} = \bar{M}_{21} = \frac{m_{i2}\alpha_2}{2} - \frac{m_{i2}{\alpha_2}^2}{3}, \tag{2.46}$$

$$\bar{M}_{22} = m + m_{i2} - m_{i2}\alpha_2 + \frac{m_{i2}{\alpha_2}^2}{3}, \tag{2.47}$$

$$\bar{m}_i = \frac{m_{i1}{\alpha_1}^2}{3} - \frac{m_{i1}\alpha_1}{2}, \tag{2.48}$$

$$\hat{k}_1 = k_1{\alpha_1}^2, \tag{2.49}$$

$$\hat{k}_2 = k_2{\alpha_2}^2. \tag{2.50}$$

Equations of motion can be written in matrix form considering input displacement (u_{i-1}) and output displacements (u_i and u_{i+1}):

$$\mathbf{M_0}\ddot{\mathbf{u}}_\mathbf{0} + \mathbf{K_0}\mathbf{u_0} = \mathbf{m_I}\ddot{u}_I + \mathbf{k_I}u_I, \tag{2.51}$$

$$\mathbf{M_0} = \begin{bmatrix} \bar{\mathrm{M}}_{11} & \bar{\mathrm{M}}_{12} \\ \bar{\mathrm{M}}_{21} & \bar{\mathrm{M}}_{22} \end{bmatrix}, \tag{2.52}$$

$$\mathbf{K_0} = \begin{bmatrix} \hat{k}_1 + \hat{k}_2 & -\hat{k}_2 \\ -\hat{k}_2 & \hat{k}_2 \end{bmatrix}, \tag{2.53}$$

$$\mathbf{m_I} = \begin{bmatrix} \bar{m}_i \\ 0 \end{bmatrix}, \tag{2.54}$$

$$\mathbf{k_I} = \begin{bmatrix} \hat{k}_1 \\ 0 \end{bmatrix}, \tag{2.55}$$

$$\ddot{\mathbf{u}}_\mathbf{0} = \begin{bmatrix} \ddot{u}_i \\ \ddot{u}_{i+1} \end{bmatrix}, \tag{2.56}$$

$$\mathbf{u_0} = \begin{bmatrix} u_i \\ u_{i+1} \end{bmatrix}, \tag{2.57}$$

$$\ddot{u}_I = \ddot{u}_{i-1}, \tag{2.58}$$

$$u_I = u_{i-1}. \tag{2.59}$$

Dynamic stiffness matrix of output (**A**) and input (**b**) can be obtained by assuming harmonic waves:

$$\mathbf{A} \equiv \mathbf{K_0} - \omega^2\mathbf{M_0}, \tag{2.60}$$

$$\mathbf{b} \equiv \mathbf{k_I} - \omega^2\mathbf{m_I}. \tag{2.61}$$

After substituting $\mathbf{A}$ and $\mathbf{b}$ into Equation (2.51), new equations of motion are obtained as

$$\mathbf{A}\mathbf{u_0} = \mathbf{b}u_I, \tag{2.62}$$

$$\mathbf{A} = \begin{bmatrix} \hat{k}_1 + \hat{k}_2 - \omega^2\overline{\mathrm{M}}_{11} & -\hat{k}_2 - \omega^2\overline{\mathrm{M}}_{12} \\ -\hat{k}_2 - \omega^2\overline{\mathrm{M}}_{21} & \hat{k}_2 - \omega^2\overline{\mathrm{M}}_{22} \end{bmatrix}, \tag{2.63}$$

$$\mathbf{b} = \begin{bmatrix} \hat{k}_1 - \omega^2\overline{m}_i \\ 0 \end{bmatrix}. \tag{2.64}$$

Transmissibility vector (TR) of this system is acquired by obtaining the ratio of output displacement to input displacement:

$$TR = \begin{bmatrix} u_i/u_{i-1} \\ u_{i+1}/u_{i-1} \end{bmatrix}, \tag{2.65}$$

$$TR = \mathbf{A}^{-1}\mathbf{b}. \tag{2.66}$$

In two lever LTTS, u_{i-1} is input displacement, u_i and u_{i+1} are output displacements but u_i is in the middle of the system and u_{i+1} is at the output boundary of the system, so transmissibility function is obtained by proportioning u_{i+1} and u_{i-1}, which is the second row of transmissibility vector (TR).

According to the second row of Equation (2.66), transmissibility graph can be obtained. Antiresonance and resonance frequency values are dependent on the system parameters, i.e., k_1, k_2, m, m_{i1}, m_{i2}, α_1 and α_2. The order of the antiresonance and resonance frequencies can be changed by varying the parameters. Although several other cases can be obtained, three different cases are shown, i.e., $\omega_{p1}<\omega_{p2}<\omega_{z1}<\omega_{z2}$, $\omega_{p1}<\omega_{p2}<\omega_{z1}=\omega_{z2}$ and $\omega_{p1}<\omega_{z1}<\omega_{z2}<\omega_{p2}$ depicted in Figure 2.18, Figure 2.19 and Figure 2.20, respectively.

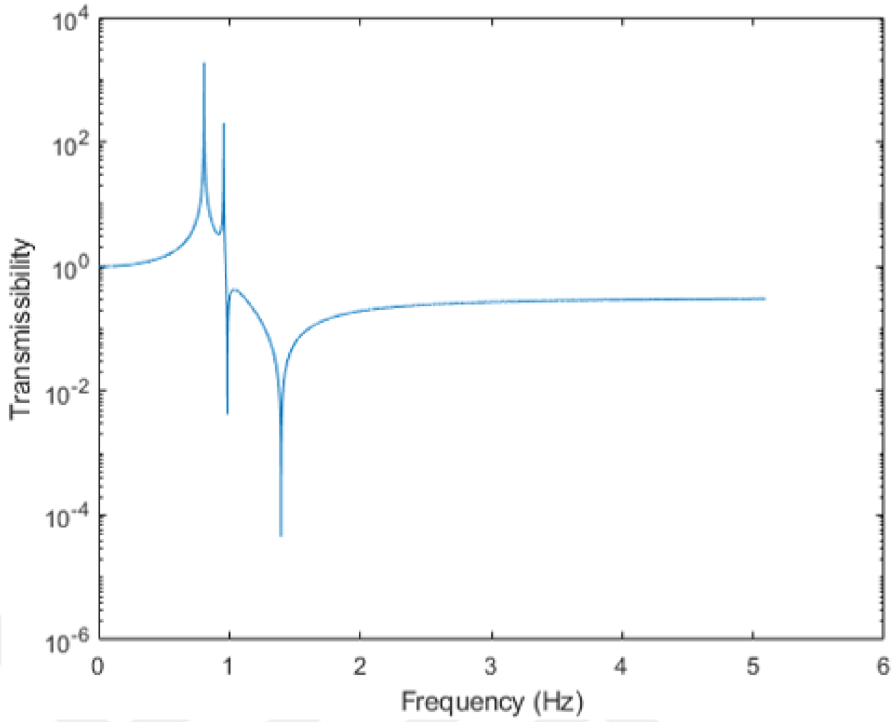

Figure 2.18. Transmissibility graph of two lever LTTS for k_1=8 N/m, k_2=4 N/m m=1kg, m_{i1}=0.5kg, m_{i2}=0.5kg, α_1=4 and α_2=4.

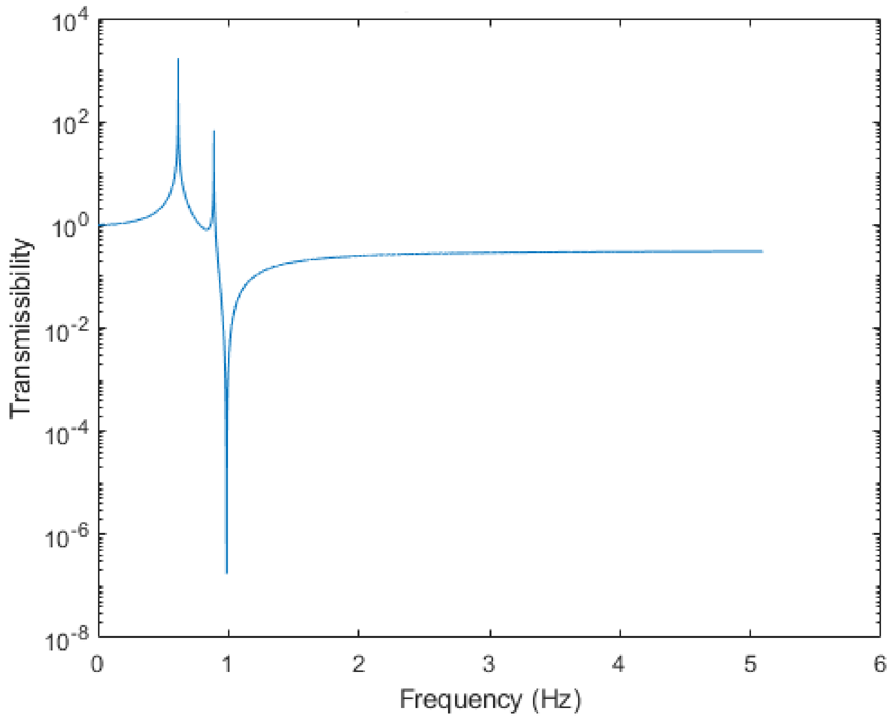

Figure 2.19. Transmissibility graph of two lever LTTS for k_1=4 N/m, k_2=4 N/m m=1kg, m_{i1}=0.5kg, m_{i2}=0.5kg, α_1=4 and α_2=4.

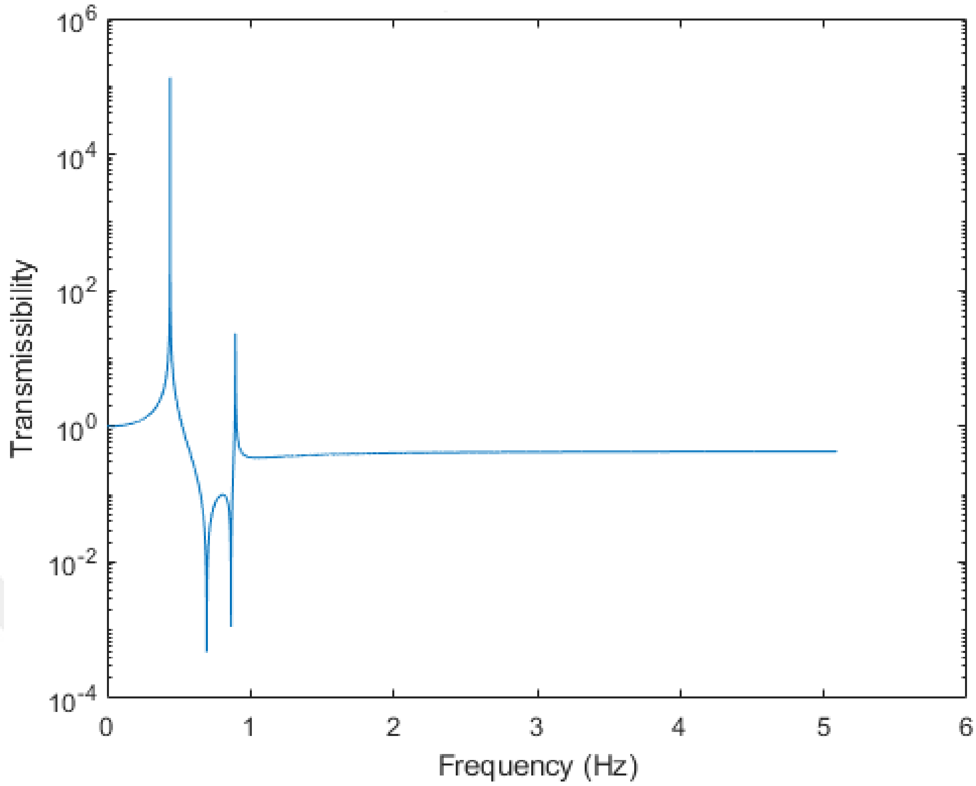

Figure 2.20. Transmissibility graph of two lever LTTS for k_1=2 N/m, k_2=4 N/m m=1kg, m_{i1}=0.5kg, m_{i2}=0.5kg, α_1=4 and α_2=8.

For low-pass filter type response, cases in Figure 2.18, Figure 2.19 can be used. Moreover, for band-stop filter type response, case in Figure 2.20 can be utilized. To obtain a wide low frequency band gap, band-stop filter type system will be used.

The parameters (m, k_1, k_2, m_{i1}, m_{i2}, α_1, α_2) affect the frequency response of the system. To examine the effect of these parameters, parametric study for each one is performed.

Two lever LTTS having different m values (m=0.25kg, 0.5kg and 1kg) are compared. m does not change antiresonance frequencies (ω_{z1}, ω_{z2}) as seen in Figure 2.21. However, first and second resonance frequencies (ω_{p1}, ω_{p2}) decrease with increasing m value.

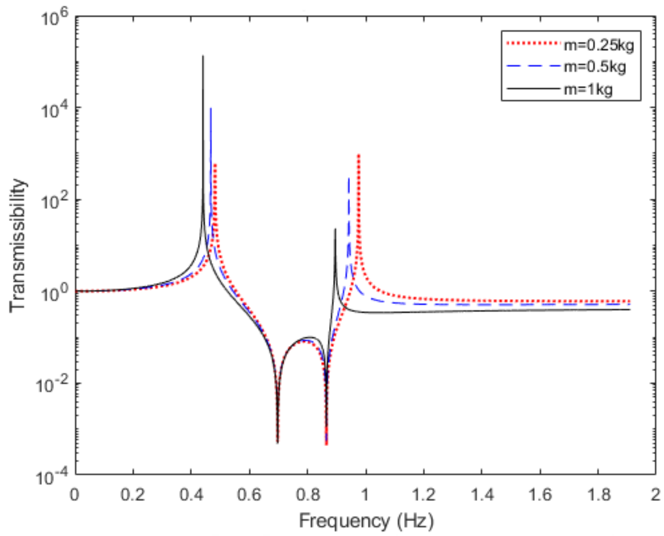

Figure 2.21. Transmissibility graph of two lever LTTS (k_1=2 N/m, k_2=4 N/m, m_{i1}=0.5kg, m_{i2}=0.5kg, α_1=4 and α_2=8) for m=0.25kg, 0.5kg and 1kg.

Two lever LTTS having different masses of first lever (m_{i1}=0.5kg, 0.75kg and 1kg) are compared. m_{i1} does not alter the second antiresonance (ω_{z2}) and second resonance (ω_{p2}) frequencies, which is depicted in Figure 2.22. Increase in m_{i1} causes decrease in the first resonance (ω_{p1}) and first antiresonance (ω_{z1}) frequencies, which is desirable to obtain wide low frequency band gap. However, attenuation level between the two antiresonance frequencies gets worse when the two antiresonance frequencies are further apart.

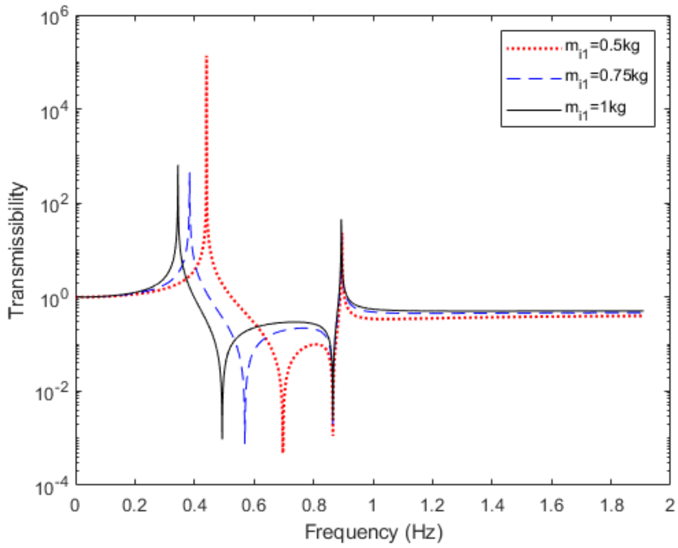

Figure 2.22. Transmissibility graph of two lever LTTS (k_1=2 N/m, k_2=4 N/m, m=1kg, m_{i2}=0.5kg, α_1=4 and α_2=8) for m_{i1}=0.5kg, 0.75kg and 1kg.

Two lever LTTS having different masses of second lever (m_{i2}=0.4kg, 0.5kg and 0.6kg) are compared. m_{i2} does not influence the first antiresonance (ω_{z1}) and first resonance (ω_{p1}) frequencies, which is indicated in Figure 2.23. Increase in m_{i2} decreases the second resonance (ω_{p2}) and second antiresonance (ω_{z2}) frequencies, which is undesirable to obtain a wide low frequency band gap. However, attenuation level between the two antiresonance frequencies improves when the two antiresonance frequencies are closer.

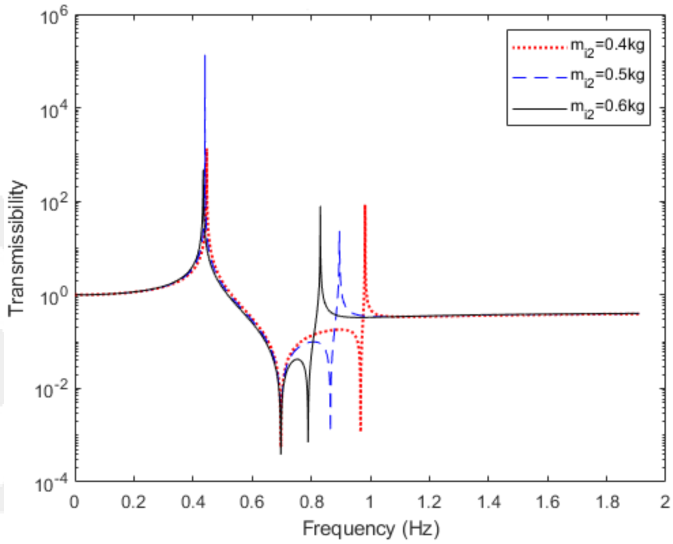

Figure 2.23. Transmissibility graph of two lever (k_1=2 N/m, k_2=4 N/m, m=1kg, m_{i1}=0.5kg, α_1=4 and α_2=8) for m_{i2}=0.4kg, 0.5kg and 0.6kg.

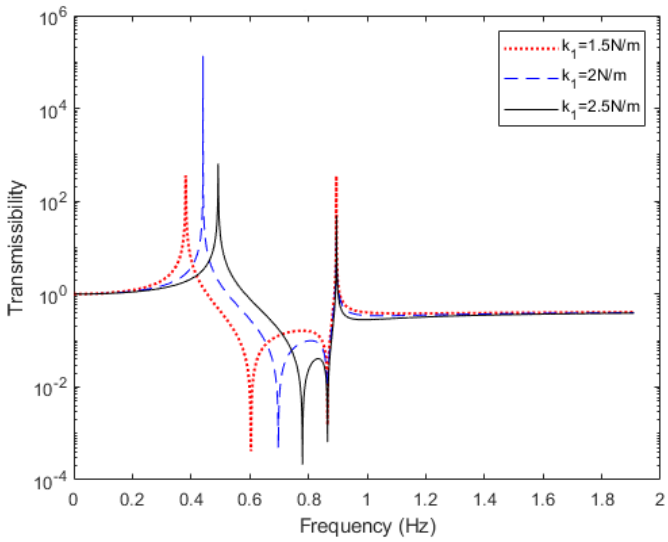

Figure 2.24. Transmissibility graph of two lever LTTS (k_2=4 N/m, m=1kg, m_{i1}=0.5kg, m_{i2}=0.5kg, α_1=4 and α_2=8) for k_1=1.5N/m, 2N/m and 2.5N/m.

Two lever LTTS having different stiffness of the first spring (k_1=1.5N/m, 2N/m and 2.5N/m) are compared. k_1 does not change the second antiresonance (ω_{z2}) and second resonance (ω_{p2}) frequencies, which is depicted in Figure 2.24. However, the first antiresonance (ω_{z1}) and first resonance (ω_{p1}) frequencies raise by increasing the first spring constant (k_1).

Two lever LTTS having different stiffness of the second spring (k_2=3N/m, 4N/m and 5N/m) are compared. k_2 does not influence the first antiresonance (ω_{z1}) and first resonance (ω_{p1}) frequencies, which is indicated in Figure 2.25. However, the second antiresonance (ω_{z2}) and second resonance (ω_{p2}) frequencies increase by increasing the second spring constant (k_2).

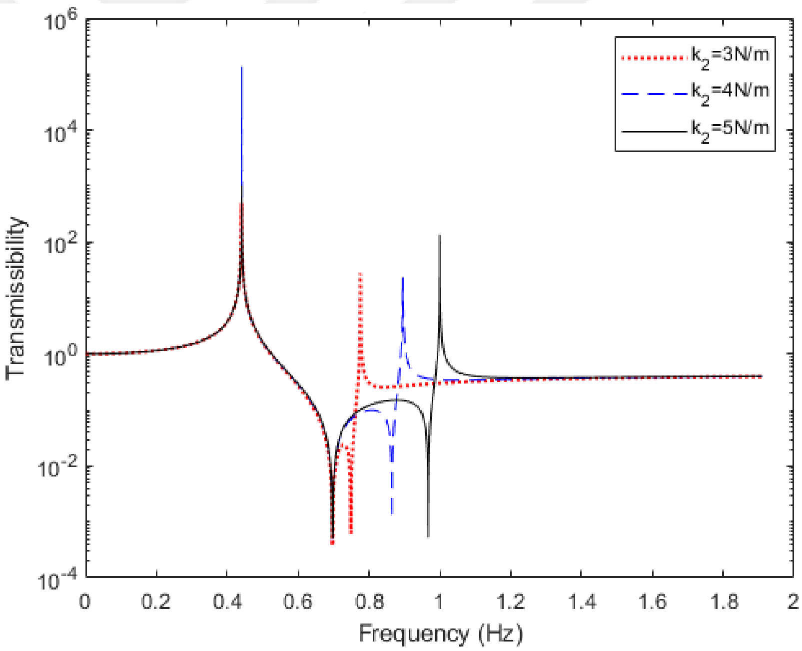

Figure 2.25. Transmissibility graph of two lever LTTS (k_1=2 N/m, m=1kg, m_{i1}=0.5kg, m_{i2}=0.5kg, α_1=4 and α_2=8) for k_1=3N/m, 4N/m and 5N/m.

Two lever LTTS having different α_1 values (α_1=3, 4 and 5) are compared. α_1 does not change the second antiresonance (ω_{z2}) and second resonance (ω_{p2}) frequencies, which is depicted in Figure 2.26. However, increase in α_1 causes increase in the first resonance frequency (ω_{p1}) and decrease in the first antiresonance frequency (ω_{z1}).

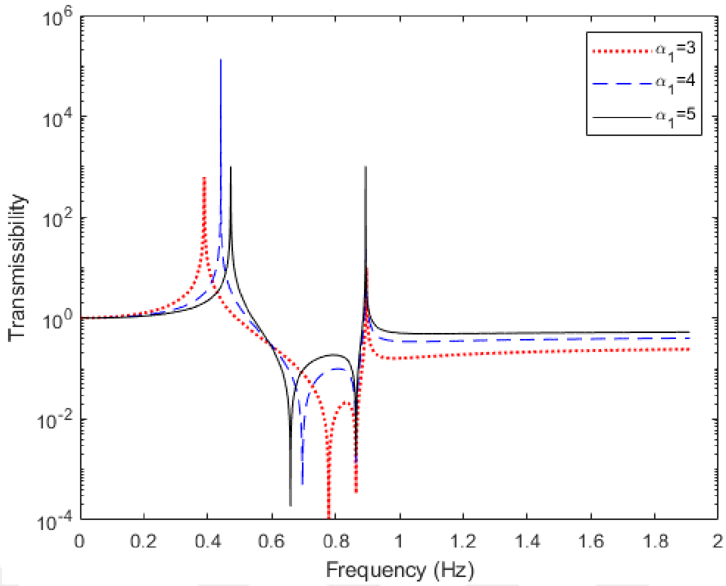

Figure 2.26. Transmissibility graph of two lever LTTS (k_1=2 N/m, k_2=4 N/m m=1kg, m_{i1}=0.5kg, m_{i2}=0.5kg and α_2=8) for α_1=3, 4 and 5.

Two lever LTTS having different α_2 values (α_2=8, 12 and 18) are compared. α_2 does not influence the first antiresonance (ω_{z1}) and first resonance (ω_{p1}) frequencies, which is indicated in Figure 2.27. The second antiresonance (ω_{z2}) and second resonance (ω_{p2}) frequencies decrease with increasing α_2.

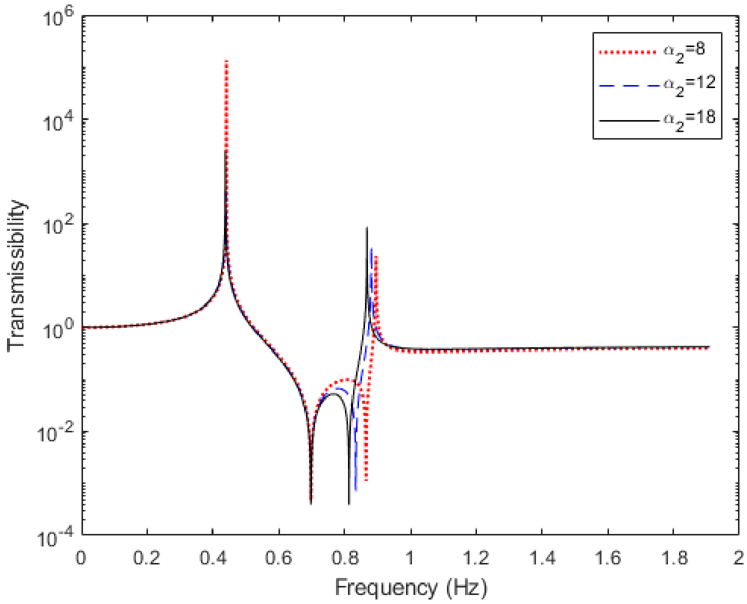

Figure 2.27. Transmissibility graph of two lever LTTS (k_1=2 N/m, k_2=4 N/m m=1kg, m_{i1}=0.5kg, m_{i2}=0.5kg and α_1=4) for α_2=8, 12 and 18.

The effect of each parameter (m, k_1, k_2, m_{i1}, m_{i2}, α_1, α_2) was examined one by one via parametric studies. To experience the total effect of all parameters, two models which are the first band-stop filter type model before parametric study shown in Figure 2.20 (m=1kg, m_{i1}=0.5kg, m_{i2}=0.5kg, k_1=2 N/m, k_2=4 N/m, α_1=4, α_2=8) and the model having the best parameter values in each parametric study (m=0.25kg, m_{i1}=1kg, m_{i2}=0.4kg, k_1=1.5 N/m, k_2=5 N/m, α_1=3, α_2=8) are compared in Figure 2.28. The second model has higher second antiresonance (ω_{z2}), resonance (ω_{p2}) frequencies and lower first antiresonance (ω_{z1}), resonance (ω_{p1}) frequencies than the first one, which provides a wider stop band compared to the first model. However, the stop band is deeper in the first model.

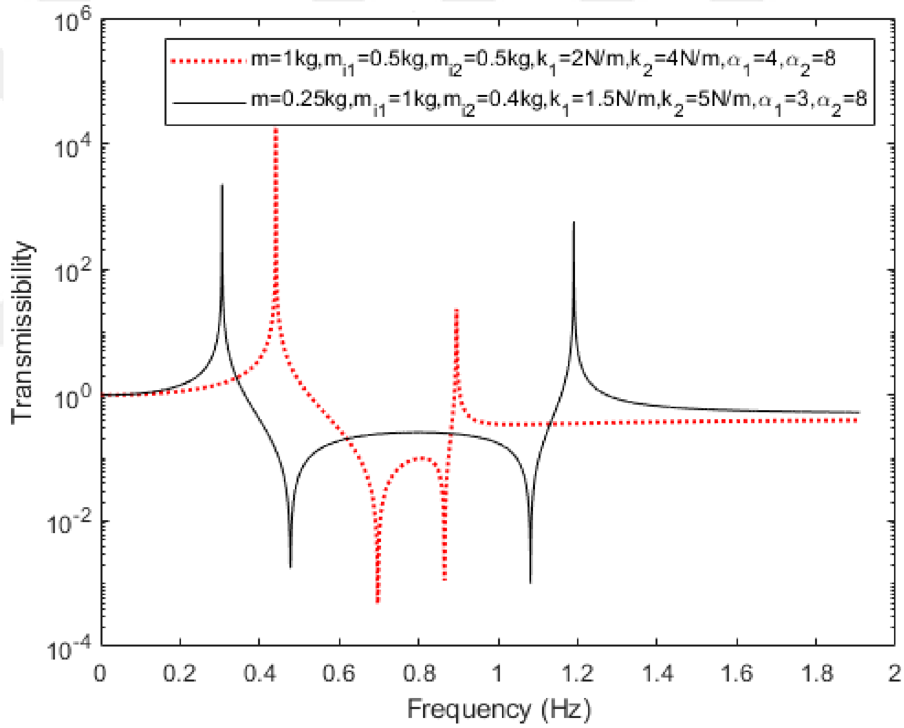

Figure 2.28. Transmissibility graph of two lever LTTS for m=1kg, m_{i1}=0.5kg, m_{i2}=0.5kg, k_1=2 N/m, k_2=4 N/m, α_1=4, α_2=8 and m=0.25kg, m_{i1}=1kg, m_{i2}=0.4kg, k_1=1.5 N/m, k_2=5 N/m, α_1=3, α_2=8.

In order to obtain a 1D lattice structure made of two lever LTTSs (Figure 2.29(a)), the unit cell in Figure 2.29(b) is used. Notice that lever dimensions are defined as in Figure 2.16(b).

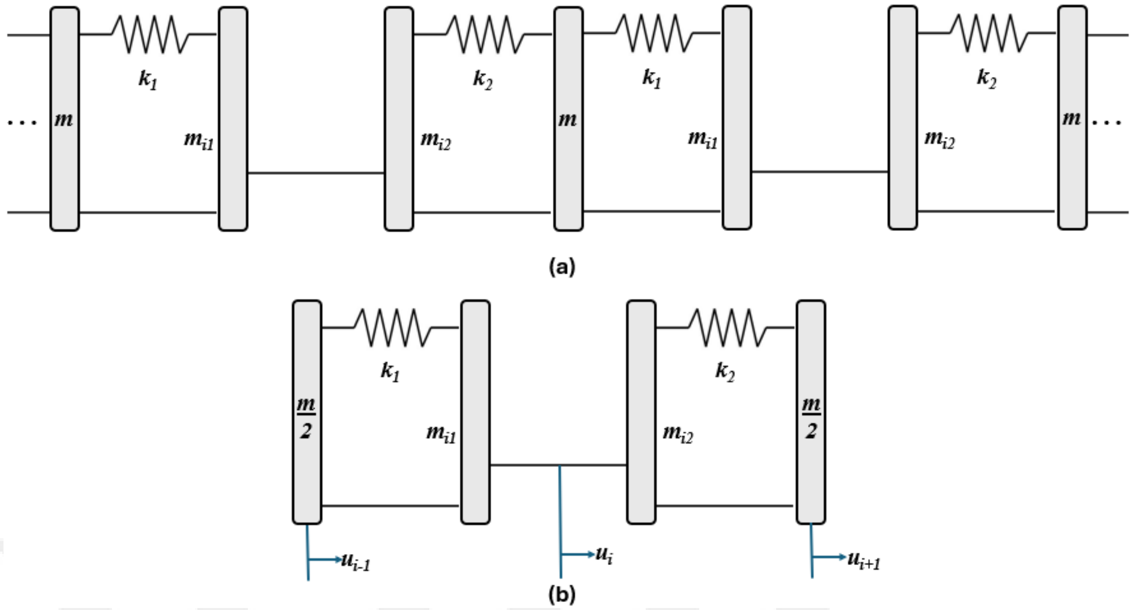

Figure 2.29 (a) 1D Periodic model of two lever LTTS (b) Two lever LTTS unit cell.

Equations of motion containing $\hat{k}_1$(Equation (2.49)) and $\hat{k}_2$(Equation (2.50)) terms for the unit cell of two lever LTTS are expressed as

$$\bar{\bar{\mathrm{M}}}_{11}\ddot{u}_{i-1} + \bar{\bar{\mathrm{M}}}_{12}\ddot{u}_i + \hat{k}_1 u_{i-1} - \hat{k}_1 u_i = 0, \tag{2.67}$$

$$\bar{\bar{\mathrm{M}}}_{21}\ddot{u}_{i-1} + \bar{\bar{\mathrm{M}}}_{22}\ddot{u}_i + \bar{\bar{\mathrm{M}}}_{23}\ddot{u}_{i+1} - \hat{k}_1 u_{i-1} + (\hat{k}_1 + \hat{k}_2)u_i - \hat{k}_2 u_{i+1} = 0, \tag{2.68}$$

$$\bar{\bar{\mathrm{M}}}_{32}\ddot{u}_i + \bar{\bar{\mathrm{M}}}_{33}\ddot{u}_{i+1} - \hat{k}_2 u_i + \hat{k}_2 u_{i+1} = 0, \tag{2.69}$$

$$\bar{\bar{\mathrm{M}}}_{11} = 0.5m + m_{i1} - m_{i1}\alpha_1 + \frac{m_{i1}{\alpha_1}^2}{3}, \tag{2.70}$$

$$\bar{\bar{\mathrm{M}}}_{12} = \bar{\bar{\mathrm{M}}}_{21} = \frac{m_{i1}\alpha_1}{2} - \frac{m_{i1}{\alpha_1}^2}{3}, \tag{2.71}$$

$$\bar{\bar{\mathrm{M}}}_{22} = \frac{m_{i1}{\alpha_1}^2}{3} + \frac{m_{i2}{\alpha_2}^2}{3}, \tag{2.72}$$

$$\bar{\bar{\mathrm{M}}}_{23} = \bar{\bar{\mathrm{M}}}_{32} = \frac{m_{i2}\alpha_2}{2} - \frac{m_{i2}{\alpha_2}^2}{3}, \tag{2.73}$$

$$\bar{\bar{\mathrm{M}}}_{33} = 0.5m + m_{i2} - m_{i2}\alpha_2 + \frac{m_{i2}{\alpha_2}^2}{3}. \tag{2.74}$$

Equations of motion can be written in matrix form considering mass matrix $\bar{\bar{\mathbf{M}}}$, stiffness matrix $\bar{\bar{\mathbf{K}}}$, displacement vector $\mathbf{u}$ and acceleration vector $\ddot{\mathbf{u}}$:

$$\bar{\bar{\mathbf{M}}}\ddot{\mathbf{u}} + \bar{\bar{\mathbf{K}}}\mathbf{u} = 0, \tag{2.75}$$

$$\bar{\bar{\mathbf{M}}} = \begin{bmatrix} \bar{\bar{\mathrm{M}}}_{11} & \bar{\bar{\mathrm{M}}}_{12} & 0 \\ \bar{\bar{\mathrm{M}}}_{21} & \bar{\bar{\mathrm{M}}}_{22} & \bar{\bar{\mathrm{M}}}_{23} \\ 0 & \bar{\bar{\mathrm{M}}}_{32} & \bar{\bar{\mathrm{M}}}_{33} \end{bmatrix}, \tag{2.76}$$

$$\bar{\bar{\mathbf{K}}} = \begin{bmatrix} \hat{k}_1 & -\hat{k}_1 & 0 \\ -\hat{k}_1 & \hat{k}_1 + \hat{k}_2 & -\hat{k}_2 \\ 0 & -\hat{k}_2 & \hat{k}_2 \end{bmatrix}, \tag{2.77}$$

$$\ddot{\mathbf{u}} = \begin{bmatrix} \ddot{u}_{i-1} \\ \ddot{u}_i \\ \ddot{u}_{i+1} \end{bmatrix}, \tag{2.78}$$

$$\mathbf{u} = \begin{bmatrix} u_{i-1} \\ u_i \\ u_{i+1} \end{bmatrix}. \tag{2.79}$$

In order to obtain the equation of motion of the infinitely periodic structure, Bloch’s Theorem can be used:

$$u_{i+1} = e^{j\gamma}u_{i-1}. \tag{2.80}$$

Displacement vector $\mathbf{u}$ transforms displacement of the nodes in the Bloch reduced coordinate $\tilde{\mathbf{u}}$ via transformation matrix $\mathbf{T}$:

$$\tilde{\mathbf{u}} = \begin{bmatrix} u_{i-1} \\ u_i \end{bmatrix}, \tag{2.81}$$

$$\mathbf{u} = \mathbf{T}\tilde{\mathbf{u}}, \tag{2.82}$$

$$\mathbf{T} = \begin{bmatrix} 1 & 0 \\ 0 & 1 \\ e^{j\gamma} & 0 \end{bmatrix}. \tag{2.83}$$

To obtain the dispersion curve, Bloch transformation is applied. Moreover, dynamic stiffness matrix **D** is obtained as

$$\mathbf{D} \equiv \mathbf{K} - \omega^2 \mathbf{M}, \tag{2.84}$$

$$\mathbf{D} = \begin{bmatrix} \hat{k}_1 - \omega^2 \overline{\overline{\mathrm{M}}}_{11} & -\hat{k}_1 - \omega^2 \overline{\overline{\mathrm{M}}}_{12} & 0 \\ -\hat{k}_1 - \omega^2 \overline{\overline{\mathrm{M}}}_{21} & \hat{k}_1 + \hat{k}_2 - \omega^2 \overline{\overline{\mathrm{M}}}_{22} & -\hat{k}_2 - \omega^2 \overline{\overline{\mathrm{M}}}_{23} \\ 0 & -\hat{k}_2 - \omega^2 \overline{\overline{\mathrm{M}}}_{32} & \hat{k}_2 - \omega^2 \overline{\overline{\mathrm{M}}}_{33} \end{bmatrix}. \tag{2.85}$$

Transformed dynamic stiffness matrix $\tilde{\mathbf{D}}$ is acquired by multiplying $\mathbf{T}^{\mathbf{H}}$ (Hermitian transpose of transformation matrix), **D** and **T**:

$$\tilde{\mathbf{D}} = \mathbf{T}^{\mathbf{H}} \mathbf{D} \mathbf{T}, \tag{2.86}$$

$$\tilde{D} = \begin{bmatrix} 1 & 0 & e^{-j\gamma} \\ 0 & 1 & 0 \end{bmatrix} \begin{bmatrix} \hat{k}_1 - \omega^2 \overline{\overline{\mathrm{M}}}_{11} & -\hat{k}_1 - \omega^2 \overline{\overline{\mathrm{M}}}_{12} & 0 \\ -\hat{k}_1 - \omega^2 \overline{\overline{\mathrm{M}}}_{21} & \hat{k}_1 + \hat{k}_2 - \omega^2 \overline{\overline{\mathrm{M}}}_{22} & -\hat{k}_2 - \omega^2 \overline{\overline{\mathrm{M}}}_{23} \\ 0 & -\hat{k}_2 - \omega^2 \overline{\overline{\mathrm{M}}}_{32} & \hat{k}_2 - \omega^2 \overline{\overline{\mathrm{M}}}_{33} \end{bmatrix} \begin{bmatrix} 1 & 0 \\ 0 & 1 \\ e^{j\gamma} & 0 \end{bmatrix}. \tag{2.87}$$

The equation that is obtained from Bloch's Transformation becomes an eigenvalue problem for a harmonic free wave motion:

$$\tilde{\mathbf{D}}(\gamma, \omega)\tilde{\mathbf{u}} = 0. \tag{2.88}$$

Dispersion curve of two lever LTTS can be obtained via solution of eigenvalue problem. According to Equation (2.88), complex band structure graphs can be obtained. For k_1=4 N/m, k_2=4 N/m, m=1kg, m_{i1}=0.5kg, m_{i2}=0.5kg, α_1=4 and α_2=4, wave vector graphs with respect to frequency (Hz) are obtained, which are indicated in Figure 2.30. Dispersion curve of low-pass filter type periodic structure (case in Figure 2.19) is obtained.

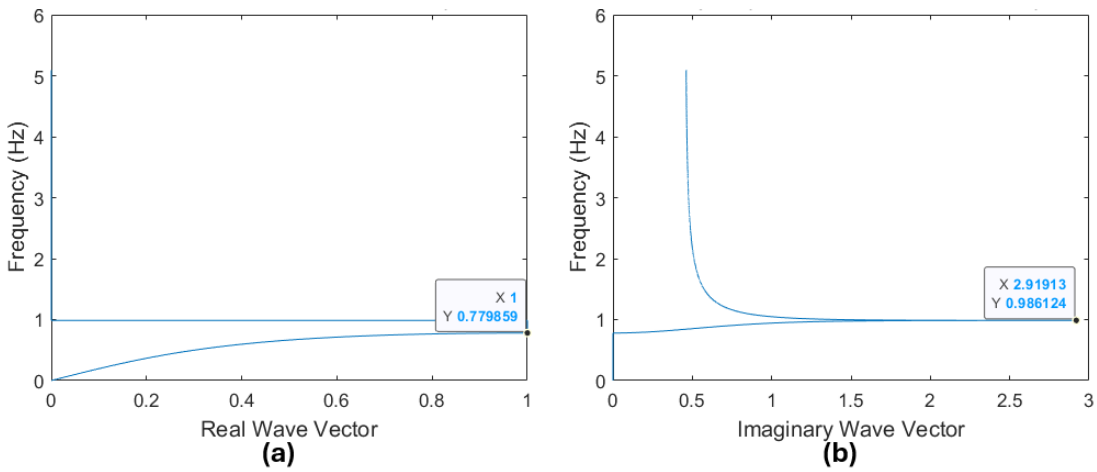

Figure 2.30. Complex band structure of the 1D periodic model generated by unit cell of two lever LTTS for k_1=4 N/m, k_2=4 N/m, m=1kg, m_{i1}=0.5kg, m_{i2}=0.5kg, α_1=4 and α_2=4 (a) Real wave vector (b) Absolute value of imaginary wave vector.

Band gap starting frequency of lattice structure is 0.78 Hz, which is lower than the notch frequency (0.98Hz) of the two lever LTTS. The notch in the imaginary part of the wave vector is due to the inertial coupling effect. Above the notch frequency, imaginary wave vector value converges to a constant value as frequency approaches infinity, which is shown in Figure 2.30(b). Imaginary part of the wave vector is related to attenuation and higher attenuation signifies a deeper band gap in a finite periodic system. Moreover, to obtain a wide low frequency band gap, band gap starting frequency should be as low as possible.

In Figure 2.30, semi-infinite band gap is divided by flat branch at 0.98 Hz. However, there is an antiresonance notch generated by inertial amplification mechanism at that frequency, which is shown in Figure 2.19.

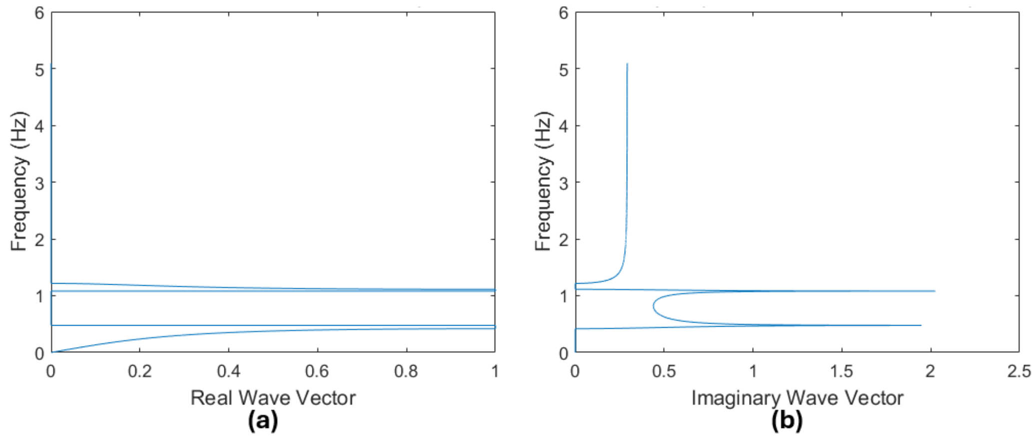

Figure 2.31. Complex band structure of the 1D periodic model generated by unit cell of two lever LTTS for m=0.25kg, m_{i1}=1kg, m_{i2}=0.4kg, k_1=1.5 N/m, k_2=5 N/m, α_1=3, α_2=8 (a) Real wave vector (b) Absolute value of imaginary wave vector.

Dispersion curve of the band-stop filter type periodic structure (two lever LTTS with m=0.25kg, m_{i1}=1kg, m_{i2}=0.4kg, k_1=1.5 N/m, k_2=5 N/m, α_1=3, α_2=8 in Figure 2.28) is obtained in Figure 2.31. A wide band gap between 0.42 - 1.11 Hz is generated. In the real wave vector plot (seen in Figure 2.31(a)), there are two flat branches at 0.48 Hz and 1.08 Hz, which divide the band gap. However, these branches are generated due to antiresonance notches at these frequencies, which are indicated in Figure 2.28. Therefore, the band gap between 0.42 - 1.11 Hz can be considered as a single band gap.

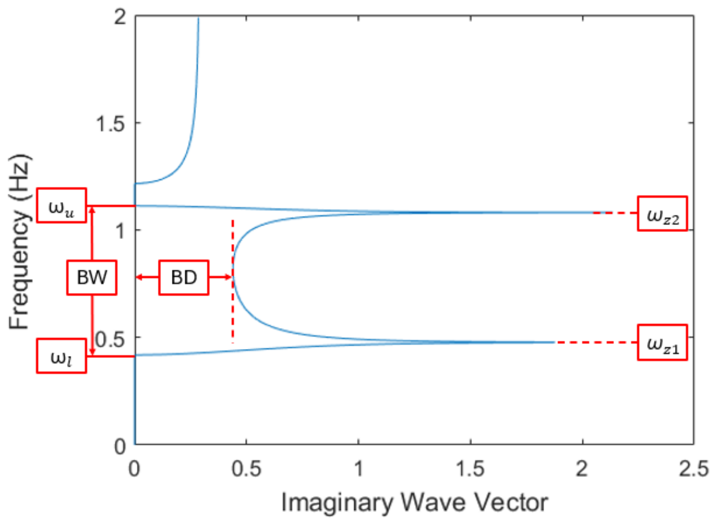

Figure 2.32. Absolute value of imaginary wave vector of the 1D periodic model generated by unit cell of two lever LTTS for m=0.25kg, m_{i1}=1kg, m_{i2}=0.4kg, k_1=1.5 N/m, k_2=5 N/m, α_1=3, α_2=8.

In Figure 2.32, the imaginary wave vector versus frequency is plotted by indicating the bandwidth (BW = $\omega_u - \omega_l$) and band depth (BD). Band depth (BD) is quantified by the minimum attenuation level between the lower antiresonance frequency (ω_{z1}) and upper antiresonance frequency (ω_{z2}). In Figure 2.33, the imaginary wave vectors are compared for the two cases in Figure 2.28. Notice that when the two antiresonance notches are further apart, the band gap is wider, however, depth of the band gap is reduced.

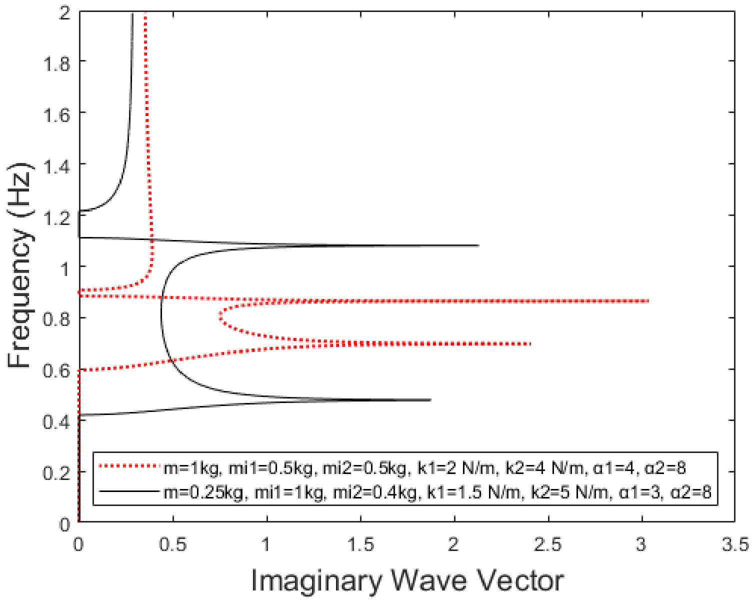

Figure 2.33. Absolute value of imaginary wave vector of the 1D periodic model generated by unit cell of two lever LTTS for m=1kg, m_{i1}=0.5kg, m_{i2}=0.5kg, k_1=2 N/m, k_2=4 N/m, α_1=4, α_2=8 and m=0.25kg, m_{i1}=1kg, m_{i2}=0.4kg, k_1=1.5 N/m, k_2=5 N/m, α_1=3, α_2=8.

To acquire a wide and deep band gap at low frequencies, optimization study is performed using the variables m, k_1, k_2, m_{i1}, m_{i2}, α_1, α_2. The objective function is to maximize the bandwidth (BW = $\omega_u - \omega_l$) given the band depth (BD = 0.2, 0.4 or 0.6). Upper limit of the band gap is set as ω_u=1 Hz. Hence, the aim is to minimize the lower limit of the band gap, i.e., ω_l. The total stiffness of the unit cell is set as k_t = 1 N/m. Moreover, total mass of the unit cell is set as m_t = 1 kg. Consequently, the optimization study can be stated as

$$\text{minimize} \qquad \omega_l, \tag{2.89}$$

subject to $BD = 0.2, 0.4 \text{ or } 0.6,$ (2.90)

$$m_t = m + m_{i1} + m_{i2}, \tag{2.91}$$

$$\frac{1}{k_t} = \frac{1}{k_1{\alpha_1}^2} + \frac{1}{k_2{\alpha_2}^2}, \tag{2.92}$$

$$m \geq 0,\ m_{i1} \geq 0,\ m_{i2} \geq 0,\ k_1 \geq 0,\ k_2 \geq 0, \tag{2.93}$$

$$\alpha_1 \geq 1, \alpha_2 \geq 1. \tag{2.94}$$

Genetic algorithm is used to solve the optimization problem. Initial results show that ω_l becomes minimum when m approaches zero and α_1, α_2 approach infinity. To obtain a realistic design, constant values are assigned to m (0.1kg) and α_1, α_2 (8).

First of all, the effects of *BD* values (0.2, 0.4 and 0.6) on optimized results according to α_1=α_2=8 are examined. Dispersion curves of 1D periodic model with optimized parameters generated by the unit cell of two lever LTTS is indicated in Figure 2.34. Upper limit of the band gap are the same for all cases and equal to 1 Hz as seen in Figure 2.34(b). Lower limit of the band gap increases with increasing *BD* indicating that band gap gets narrower.

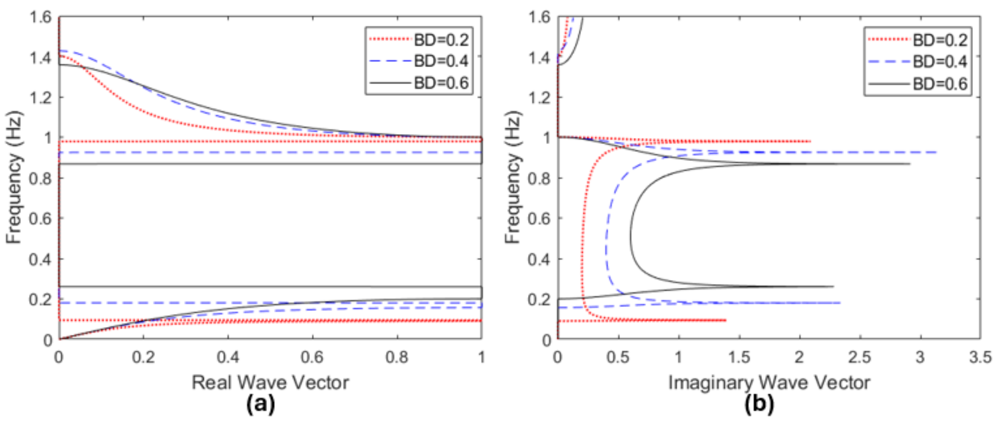

Figure 2.34. Complex band structure of the 1D periodic model with optimized parameters generated by unit cell of two lever LTTS for *BD* = 0.2, 0.4 and 0.6 (a) Real wave vector (b) Absolute value of imaginary wave vector.

Transmissibility graph of two lever LTTS with optimized parameters is shown in Figure 2.35. As the band depth (*BD*) increases, the antiresonance frequencies get closer to each other, which decreases width of the band gap.

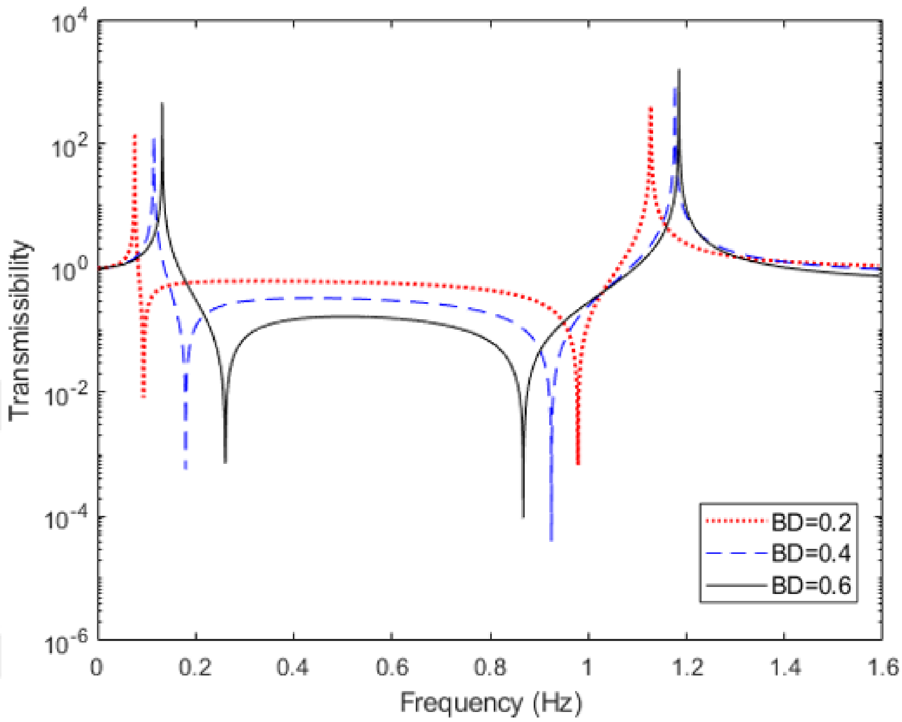

Figure 2.35. Transmissibility graph of two lever LTTS with optimized parameters for *BD* = 0.2, 0.4 and 0.6.

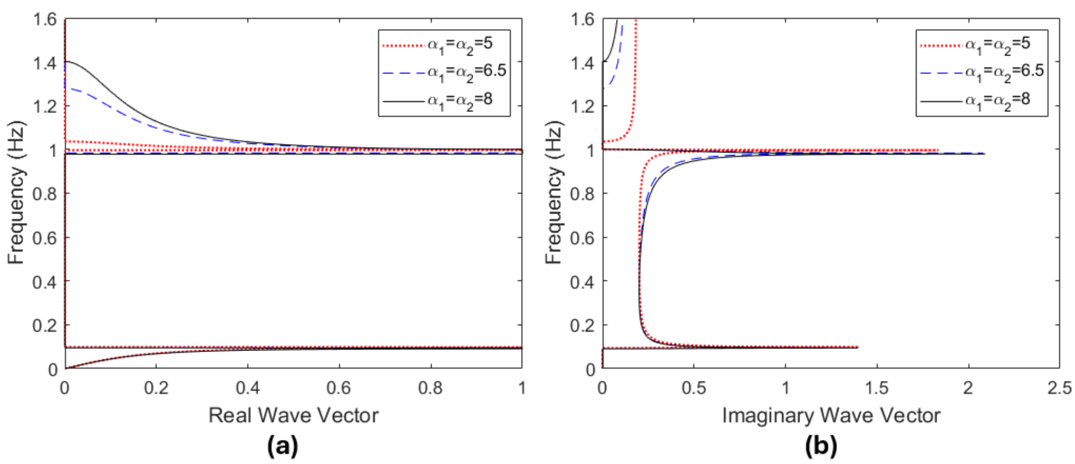

Figure 2.36. Complex band structure of the 1D periodic model with optimized parameters generated by unit cell of two lever LTTS for α_1=α_2=5, 6.5 and 8 (a) Real wave vector (b) Absolute value of imaginary wave vector.

Secondly, the effects of α_1 and α_2 values (5, 6.5 and 8) on the optimization results according to BD = 0.2 are examined. While upper limit of the band gap is constant (1 Hz), lower limit decreases very slightly with increasing α_1 and α_2 values as seen in Figure 2.36.

The effects of α_1 and α_2 values on the optimization results for different BD values are examined. As depicted in Figure 2.37, increase in α_1 and α_2 values decreases the lower limit of the band gap slightly yielding a little wider band gap. As α_1 and α_2 get larger, manufacturability of the optimum model can be difficult. Besides, there is very slight increase in the bandwidth.

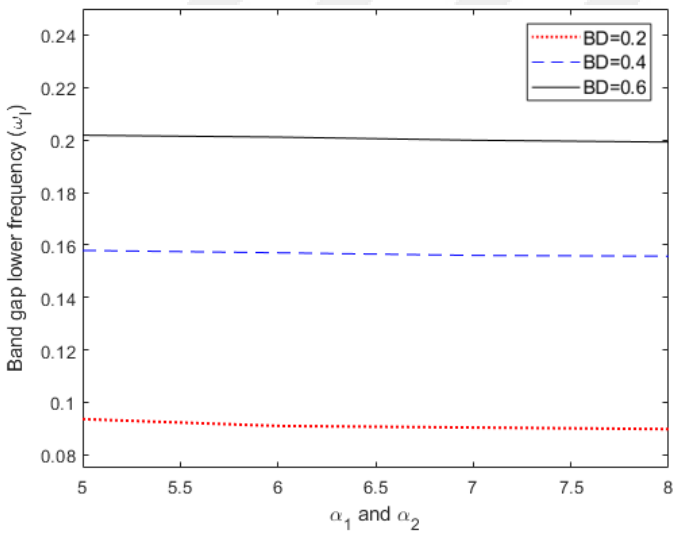

Figure 2.37. Change in the lower limit of the band gap (ω_l) due to change in α_1 and α_2 for BD = 0.2, 0.4 and 0.6

For the manufacturing stage, an optimum design should be selected by considering a reasonable upper limit for the amplification ratios. Large α_1 and α_2 values provide slight benefit for obtaining a wide band gap, but realizing very high lever ratios may not be feasible. Therefore, α_1 and α_2 are selected as "5" for the prototype. As before, m is set as "0.1 kg" and band depth (BD) is selected as "0.2". Optimized parameters according to these inputs are m=0.1kg, m_{i1}=0.452kg, m_{i2}=0.447kg, k_1=0.040N/m, k_2=4.091N/m, α_1=5 and α_2=5.

Dispersion curve of 1D periodic model of the optimum manufacturable design is indicated in Figure 2.38. The ratio of ω_u/ω_l is achieved as 10.7, which indicates a very wide band gap. The flat branches as seen in Figure 2.38(a) are generated because of antiresonance notches at these frequencies, so these two flat branches do not divide band gap.

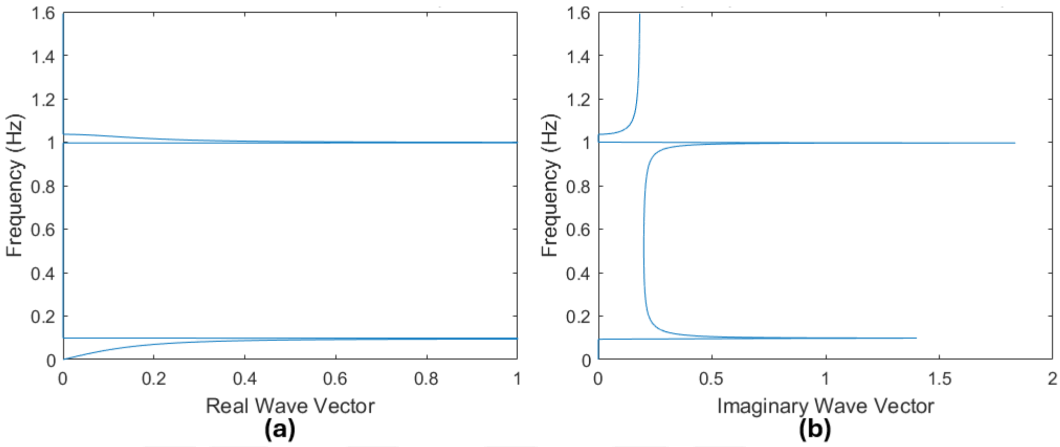

Figure 2.38. Complex band structure of the 1D periodic model with optimum design parameters generated by unit cell of two lever LTTS (m=0.1kg, m_{i1}=0.452kg, m_{i2}=0.447kg, k_1=0.040N/m, k_2=4.091N/m, α_1=5 and α_2=5) (a) Real wave vector (b) Absolute value of imaginary wave vector.

Transmissibility graph of two lever LTTS with optimized parameters is indicated in Figure 2.39.

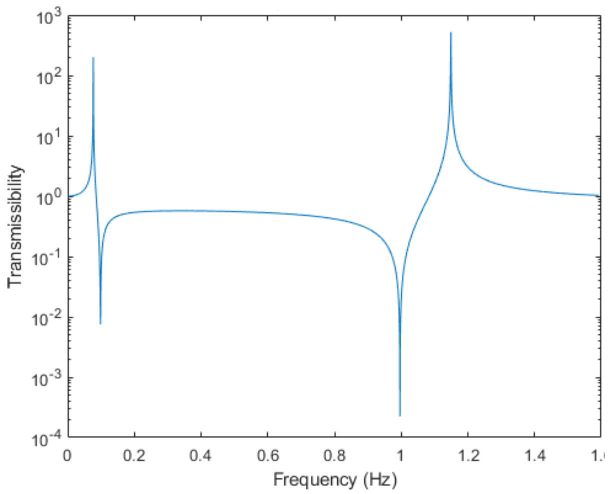

Figure 2.39. Transmissibility graph of two lever LTTS with optimum design parameters (m=0.1kg, m_{i1}=0.452kg, m_{i2}=0.447kg, k_1=0.040N/m, k_2=4.091N/m, α_1=5 and α_2=5).

Upper and lower frequency limits of the band gap in the optimum design can be scaled up or down while preserving their ratio (ω_u/ω_l). To that end, all the masses can be divided by c_1 and all the stiffnesses can be multiplied by c_2 which in turn will multiply the upper and lower limits of the band gap by $\sqrt{c_1 c_2}$, where c_1 and c_2 are positive constants. For instance, considering the optimum design in Figure 2.38, when all masses of optimum design parameters are divided by 10 (m=0.01kg, m_{i1}=0.045kg, m_{i2}=0.044kg) and all stiffnesses of optimum design parameters are multiplied by 640 (k_1=25.6N/m, k_2=2618.2N/m), upper and lower band gap limits are scaled up by 80, as depicted in Figure 2.40.

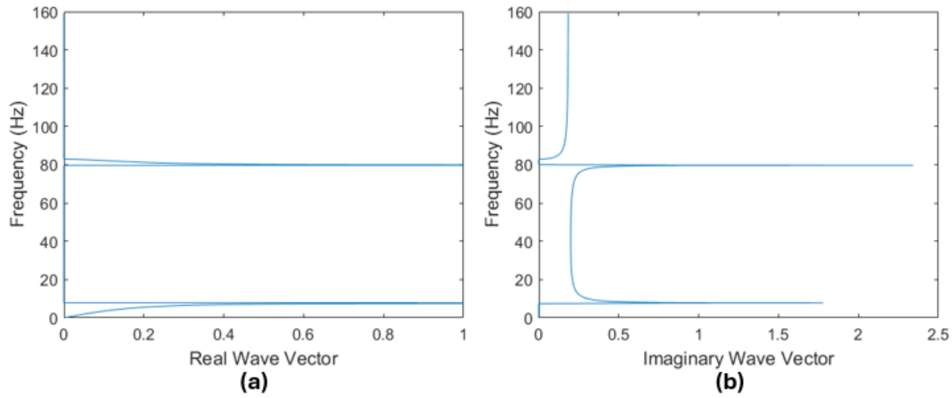

Figure 2.40. Complex band structure of the 1D periodic model with scaled design parameters generated by unit cell of two lever LTTS (m=0.01kg, m_{i1}=0.045kg, m_{i2}=0.044kg, k_1=25.6N/m, k_2=2618.2N/m, α_1=5 and α_2=5) (a) Real wave vector (b) Absolute value of imaginary wave vector.

According to optimized parameters (m=0.1kg, m_{i1}=0.452kg, m_{i2}=0.447kg, k_1=0.040N/m, k_2=4.091N/m, α_1=5 and α_2=5) obtained from genetic algorithm, a prototype will be produced. For the prototype model, mass ratios (m_{i1}/m, m_{i2}/m), stiffness ratio (k_1/k_2) and α_1 and α_2 values are important to get a ω_u/ω_l ratio close to 10 as in the optimized model. However, mass and stiffness values will be scaled so that a band gap approximately between 8 Hz and 80 Hz will be obtained. Parameters for the prototype are m=0.0074kg, m_{i1}=0.041kg, m_{i2}=0.041kg, k_1=26N/m, k_2=2500N/m, α_1=5 and α_2=5. In the optimized model, there was a constraint on m (0.1kg). When this constraint is released, ω_u/ω_l ratio can be slightly improved. Stiffness ratios are quite similar in the optimized and prototype models. Moreover, α_1 and α_2 values of the prototype are the same with the optimized model.

Dispersion curve of 1D periodic model of the prototype is depicted in Figure 2.41. ω_u and ω_l are 7.9 Hz and 81.8 Hz, respectively. The ratio of ω_u/ω_l is achieved as 10.4, which indicates a very wide band gap. The flat branches seen in Figure 2.41(a) are generated because of the antiresonance notches at these frequencies, so these two flat branches do not divide the band gap.

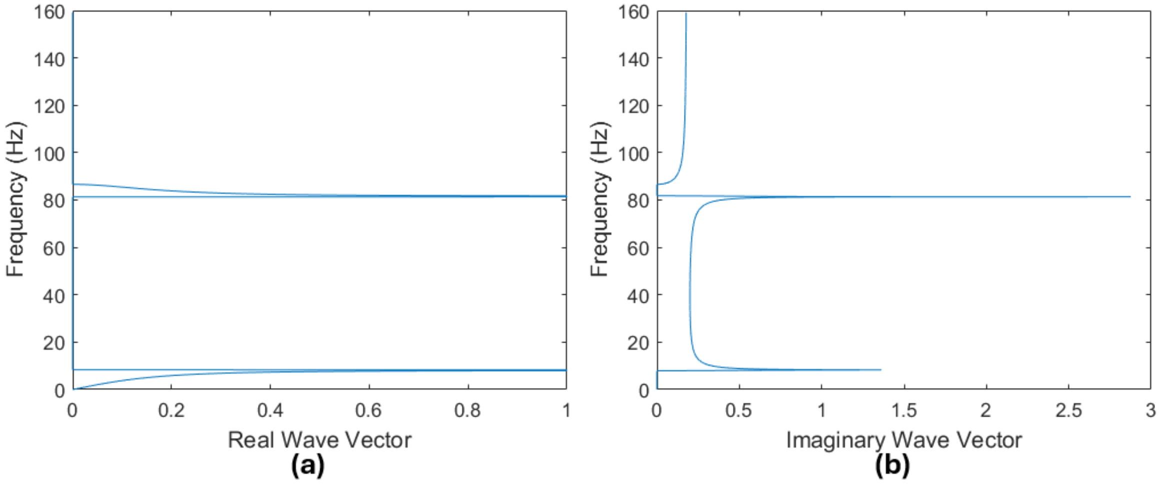

Figure 2.41. Complex band structure of the 1D periodic model of the prototype parameters generated by unit cell of two lever LTTS (m=0.0074kg, m_{i1}=0.041kg, m_{i2}=0.041kg, k_1=26N/m, k_2=2500N/m, α_1=5 and α_2=5) (a) Real wave vector (b) Absolute value of imaginary wave vector.

The prototype of two lever LTTS consisting of two unit cells will be produced for testing. This prototype will be mounted on a test fixture by two springs with stiffness k_{end}=115N/m, which is depicted in Figure 2.42.

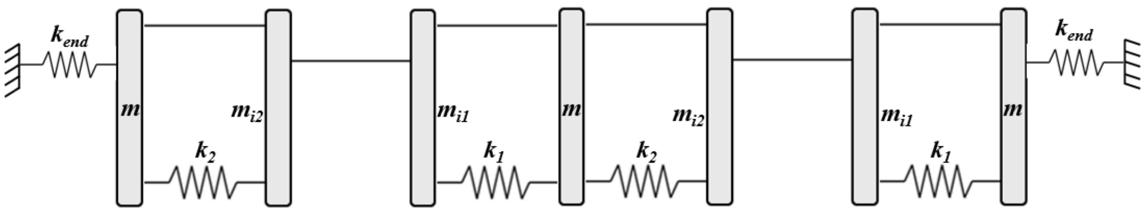

Figure 2.42. Prototype model of the two lever LTTS consisting of two unit cells.

The prototype will be hit by an impact hammer from one side and the velocity at the other side will be measured by a laser vibrometer. Hence, frequency response will be quantified by output velocity per unit input force. Analytical frequency response of the prototype model of two lever LTTS consisting of two unit cells is shown in Figure 2.43. Notice that due to the end springs, there is an extra resonance within the band gap at 12.5 Hz. Moreover, the resonance peak at 82.1 Hz is negligibly small. Consequently, there is a large stop band between 12.5 Hz and 105.2 Hz.

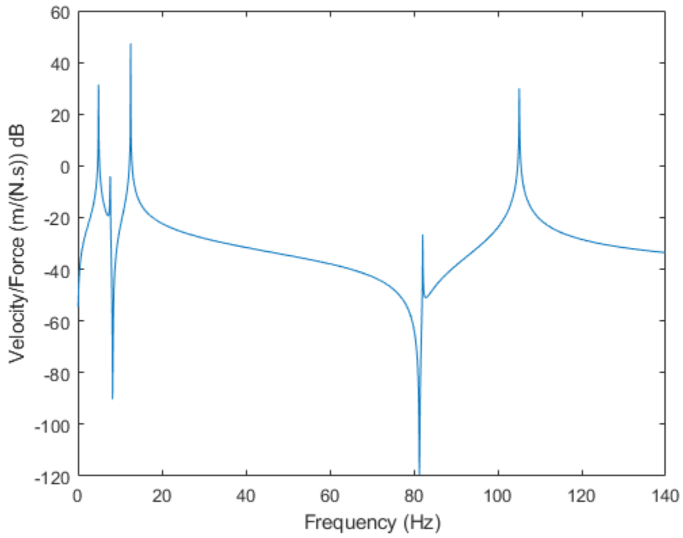

Figure 2.43. Velocity output per unit input force graph of the prototype model of two lever LTTS consisting of two unit cells (m=0.0074kg, m_{i1}=0.041kg, m_{i2}=0.041kg, k_1=26N/m, k_2=2500N/m, α_1=5 and α_2=5).

To show the effect of damping on the model, response of the system containing stiffness proportional dampers are placed parallel to k_{end}, k_1 and k_2 is examined. Velocity output per unit input force graph of prototype model of two lever LTTS consisting of two unit cells with different damping values is shown in Figure 2.44. As the stiffness proportional damping increases, magnitude of the second antiresonance notch and the fourth major resonance peak significantly decreases. Moreover, the resonance peak at 82.1 Hz is vanished with increasing damping.

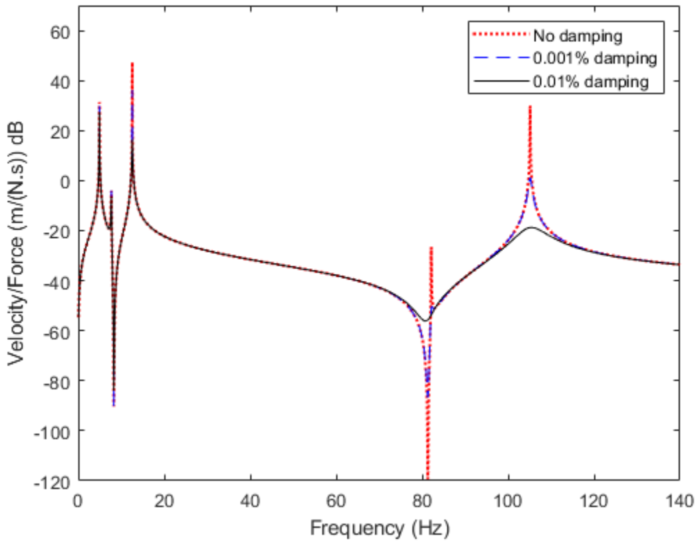

Figure 2.44. Velocity output per unit input force graph of the prototype model of two lever LTTS consisting of two unit cells for no damping, 0.001% and 0.01% stiffness proportional damping (m=0.0074kg, m_{i1}=0.041kg, m_{i2}=0.041kg, k_1=26N/m, k_2=2500N/m, α_1=5 and α_2=5).

3. EXPERIMENTAL VALIDATION

A prototype with m=0.0074kg, m_{i1}=0.041kg, m_{i2}=0.041kg, k_1=26N/m, k_2=2500N/m, k_{end}=115N/m, α_1=5 and α_2=5 depicted in Figure 2.42 is manufactured for experimental validation. The mass m is realized by using an aluminum tube whereas the masses m_{i1} and m_{i2} are made up from rectangular aluminum bars. All of these masses have a length of 10cm. Stiff polyester strings are used to combine all the levers and masses. Moreover, steel helical tension springs are used to realize k_1, k_2 and k_{end}. The tensegrity structure with two unit cells is subject to initial tension so that the levers are parallel to each other. The attachment of the strings to the levers are arranged to obtain the desired α_1 and α_2 value of 5.

To verify vibration isolation performance of two lever LTTS consisting of two unit cells, test setup depicted in Figure 3.1 is prepared. In this experiment, the prototype is excited by a hammer at the left side and velocity data is collected at the right side. The laser focus point at the output location is shown in Figure 3.1 and velocity at that location is measured via the laser vibrometer. Data acquisition system transmits the collected data to the computer. Finally, test results are displayed on the computer.

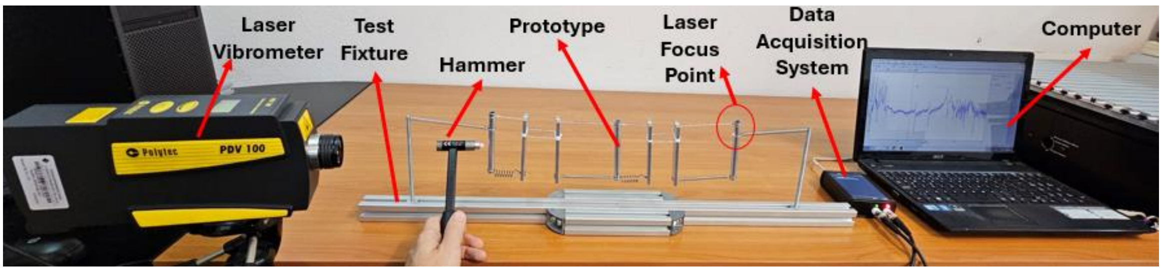

Figure 3.1. Test setup of two lever LTTS consisting of two unit cells.

The experimental frequency response of the prototype can be seen in Figure 3.2. Vibration isolation behavior of the prototype is similar to the analytical result shown in Figure 2.43.

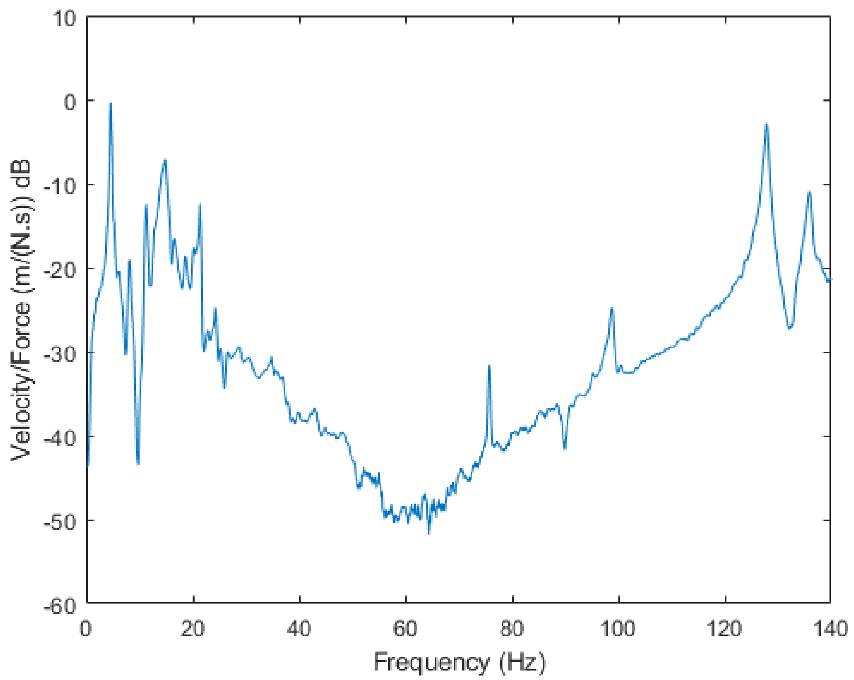

Figure 3.2. Experimental frequency response result of the two lever LTTS consisting of two unit cells.

Comparison between analytical and experimental results is depicted in Figure 3.3. To match the major resonance peak values in the analytical model with the experimental ones, dampers are placed parallel to k_1, k_2 and k_{end} as c_1=0.026 N.s/m, c_2=0.025 N.s/m and c_{end}=0.345 N.s/m, respectively. In the analytical model, the limiting resonance frequencies for the stop band are 12.5 Hz and 105.2 Hz. On the other hand, in the experimental result, the limiting resonance frequencies for the stop band are 14.5 Hz and 127.8 Hz. Although there is a shift in the stop band frequency limits, ratio of upper and lower frequency limits in these two cases are close (8.4 vs. 8.8). Below 20 Hz, there are two major resonance and one antiresonance frequencies for both analytical and experimental frequency response plots. Moreover, the order of these frequencies is also the same, i.e., the first antiresonance frequency is between the first and second major resonance frequencies. In addition, order of the second antiresonance and third major resonance frequencies are the same for both cases.

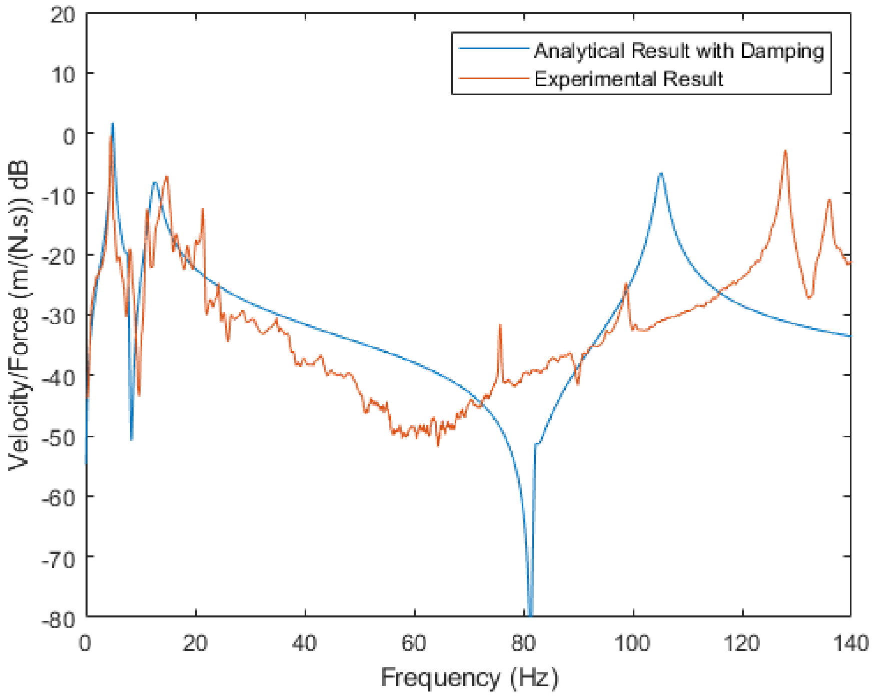

Figure 3.3. Analytical frequency response result with c_1=0.026 N.s/m, c_2=0.025 N.s/m, c_{end}=0.345 N.s/m and experimental result of the two lever LTTS consisting of two unit cells.

In the analytical model, there are several assumptions: the strings are inextensible, sagging of the structure due to gravity is negligible, test fixture provides fixed boundary conditions for the end springs (k_{end}) and prototype springs (k_1 and k_2) are assumed to have pin boundary conditions with the masses. However, the strings can slightly extend. The whole structure sags slightly due to gravity. The connections of the end springs (k_{end}) can slightly flex. Furthermore, prototype springs (k_1 and k_2) provide some resistance to bending. Despite these differences, general characteristics of the analytical and experimental frequency response curves are quite similar.

4. CONCLUSION

In this thesis, novel tensegrity structures with embedded inertial amplification mechanisms are designed and optimized for obtaining wide and deep low frequency band gaps. Two different designs, which are one lever LTTS and two lever LTTS, are introduced. First of all, analytical models of these designs and also periodic structures generated by these designs are examined. Analytical equations of both models are derived. Parametric studies are conducted to see how the system parameters affect the resonance and antiresonance frequencies of the one lever and two lever LTTSs. Optimization studies are conducted via genetic algorithm to maximize bandwidth for various band depth constraints. In order to attain a manufacturable design, constraints are stated for maximum amplification ratios and minimum mass values of individual elements. In the end, a very wide band gap is achieved whose upper and lower limits have a ratio more than 10. A prototype is manufactured for experimental validation purpose. It is seen that the analytical and experimental frequency responses show similar behavior.

As future work, this study that focuses on 1D periodic structures can be extended to 2D and 3D periodic structures. In that case, vibrations coming from multiple axes can be isolated.

REFERENCES

1. D. Sutter-Widmer, S. Deloudi and W. Steurer, "Prediction of Bragg-Scattering-Induced Band Gaps in Phononic Quasicrystals”, *Physical Review B,* vol. 75, no. 9, pp. 094304, 2007.

2. I. H. Deutsch, R. Spreeuw, S. Rolston and W. Phillips, "Photonic Band Gaps in Optical Lattices”, *Physical Review A,* vol. 52, no. 2, pp. 1394, 1995.

3. Y. Ye, C. Mei, L. Li, X. Wang, L. Ling and Y. Hu, "Broadening Band Gaps of Bragg Scattering Phononic Crystal With Graded Supercell Configuration”, *Journal of Vibration and Acoustics,* vol. 144, no. 6, pp. 061010, 2022.

4. C. Cai, Z. Wang, Y. Chu, G. Liu and Z. Xu, "The Phononic Band Gaps of Bragg Scattering and Locally Resonant Pentamode Metamaterials”, *Journal of Physics D: Applied Physics*, vol. 50, no. 41, pp. 415105, 2017.

5. M. Oudich, Y. Li, B. M. Assouar and Z. Hou, "A Sonic Band Gap Based on the Locally Resonant Phononic Plates with Stubs”, *New Journal of Physics,* vol. 12, no. 8, pp. 083049, 2010.

6. M. Moscatelli, R. Ardito, L. Driemeier and C. Comi, "Band-gap Structure in Two- and Three-dimensional Cellular Locally Resonant Materials”, *Journal of Sound and Vibration*, vol. 454, pp. 73-84, 2019.

7. P. Wang, F. Casadei, S. H. Kang and K. Bertoldi, "Locally Resonant Band Gaps in Periodic Beam Lattices by Tuning Connectivity”, *Physical Review B,* vol. 91, no. 2, pp. 020103, 2015.

8. J.-C. Hsu, "Local Resonances-induced Low-frequency Band Gaps in Two-dimensional Phononic Crystal Slabs with Periodic Stepped Resonators”, *Journal of Physics D: Applied Physics,* vol. 44, no. 5, pp. 055401, 2011.

9. M. Chen, D. Meng, H. Zhang, H. Jiang and Y. Wang, "Resonance-coupling Effect on Broad Band Gap Formation in Locally Resonant Sonic Metamaterials”, *Wave Motion,* vol. 63, pp. 111-119, 2016.

10. M. Miniaci, M. Mazzotti, A. Amendola and F. Fraternali, "Effect of Prestress on Phononic Band Gaps Induced by Inertial Amplification”, *International Journal of Solids and Structures,* vol. 216, pp. 156-166, 2021.

11. J. Li, P. Yang and S. Li, "Phononic Band Gaps by Inertial Amplification Mechanisms in Periodic Composite Sandwich Beam with Lattice Truss Cores”, *Composite Structures,* vol. 231, pp. 111458, 2020.

12. A. Banerjee, S. Adhikari and M. I. Hussein, "Inertial Amplification Band-gap Generation by Coupling a Levered Mass with Locally Resonant Mass”, *International Journal of Mechanical Sciences,* vol. 207, pp. 106630, 2021.

13. T. Delpero, G. Hannema, B. V. Damme, S. Schoenwald, A. Zemp and A. Bergamini, "Inertia Amplification in Phononic Crystals for Low Frequency Bandgaps”, *8 ECCOMAS SMART,* vol. 2017, pp. 1657-1668, 2017.

14. J. Li, P. Yang and S. Li, "Multiple Band Gaps for Efficient Wave Attenuation by Inertial Amplification in Periodic Functionally Graded Beams”, *Composite Structures,* vol. 271, pp. 114130, 2021.

15. W. Ding, R. Zhang, T. Chen, S. Qu, D. Yu, L. Dong, J. Zhhu, Y. Yang and B. Assouar, "Origin and Tuning of Bandgap in Chiral Phononic Crystals", *Communications Physics*, vol. 7, no. 1, pp. 272, 2024.

16. L. Gao, C. M. Mak, K. W. Ma and C. Cai, "Mechanisms of Multi-bandgap Inertial Amplification Applied in Metamaterial Sandwich Plates", *International Journal of Mechanical Sciences* , vol. 277, pp. 109424, 2024.

17. J. Li and S. Li, "Generating Ultra Wide Low-frequency Gap for Transverse Wave Isolation via Inertial Amplification Effects", *Physics Letters A*, vol. 382, no. 5, pp. 241-247, 2018.

18. O. Yüksel and Ç. Yılmaz, "Shape Optimization of Phononic Band Gap Structures Incorporating Inertial Amplification Mechanisms", *Journal of Sound and Vibration*, vol. 355, pp. 232-245, 2015.

19. K. Kocak and Ç. Yılmaz, "Design of a Compliant Lever-type Passive Vibration Isolator with Quasi-zero-stiffness Mechanism", *Journal of Sound and Vibration*, vol. 558, pp. 117758, 2023.

20. C. Goffaux, F. Maseri, J. O. Vasseur, B. Djafari-Rouhani and P. Lambin, "Measurements and Calculations of the Sound Attenuation by a Phononic Band Gap Structure Suitable for an Insulating Partition Application", *Applied Physics Letters*, vol. 83, no. 2, pp. 281-283, 2003.

21. J. Li, X. Wu, C. Wang and Q. Huang, "Sound Insulation Prediction and Band Gap Characteristics of Four Vibrators Acoustic Metamaterial with Composite Phononic Crystal Structure", *Materials Today Communications* , vol. 37, pp. 107455, 2023.

22. C. Guillén-Gallegos, H. Alva-Medrano, H. Pérez-Aguilar, A. Mendoza-Suárez and F. Villa-Villa, "Phononic Band Structure of an Acoustic Waveguide that Behaves as a Phononic Crystal”, *Results in Physics,* vol. 12, pp. 1111-1118, 2019.

23. Z. Jia, Y. Bao, Y. Luo, D. Wang, X. Zhang and Z. Kang, "Maximizing Acoustic Band Gap in Phononic Crystals via Topology Optimization”, *International Journal of Mechanical Sciences,* vol. 270, pp. 109107, 2024.

24. Z. Jia, Y. Chen, H. Yang and L. Wang, "Designing Phononic Crystals with Wide and Robust Band Gaps”, *Physical Review Applied,* vol. 9, no. 4, pp. 044021, 2018.

25. L. Zhang, J. R. Li, J. C. Guo and Z. Zhang, "Band Gap Design of Beam-Supported Phononic Crystal by Regulation and Control of Beam Bending Stifness”, *Journal of Vibration Engineering & Technologies,* vol. 12, no. 2, pp. 1649-1658, 2024.

26. X. Zhou, Y. Xu, Y. Liu, L. Lv, F. Peng and L. Wang, "Extending and Lowering Band Gaps by Multilayered Locally Resonant Phononic Crystals”, *Applied Acoustics,* vol. 133, pp. 97-106, 2018.

27. G. Wang, S. Wan, J. Hong , S. Liu and X. Li, "Analysis of Flexural and Torsional Vibration Band Gaps in Phononic Crystal Beam”, *Journal of Vibration and Control,* vol. 29, no. 19-20, pp. 4814-4827, 2023.

28. Y. Xin, P. Cai, P. Li, Y. Qun, Y. Sun, D. Qian, S. Cheng and Q. Zhao, "Comprehensive Analysis of Band Gap of Phononic Crystal Structure and Objective Optimization Based on Genetic Algorithm”, *Physica B: Condensed Matter,* vol. 667, pp. 415157, 2023.

29. Z. Zhang, Z. Zhang and X. Jin, "Investigation on Band Gap Mechanism and Vibration Attenuation Characteristics of Cantilever-beam-type Power-exponent

Prismatic Phononic Crystal Plates”, *Applied Acoustics,* vol. 206, pp. 109314, 2023.

30. D. Yu, J. Wen, H. Zhao, Y. Liu and X. Wen, "Vibration Reduction by Using The Idea of Phononic Crystals in a Pipe-conveying Fluid”, *Journal of Sound and Vibration,* vol. 318, no. 1-2, pp. 193-205, 2008.

31. S. Gonella, A. C. To and W. K. Liu, "Interplay between Phononic Bandgaps and Piezoelectric Microstructures for Energy Harvesting”, *Journal of the Mechanics and Physics of Solids,* vol. 57, no. 3, pp. 621-633, 2009.

32. S. Haid, B. Bouadjemi, K. Azil, T. Lantri, M. Houari, M. Matougui and S. Bentata, "Numerical Assessment of Physical Properties of Ba2DyTaO6 Ferroelectric Rare Earth-Based Compound and Estimation of the Curie Temperature for Energy Harvesting and Spintronic Applications”, *Journal of Electronic Materials,* vol. 53, no. 1, pp. 75-85, 2024.

33. Z. Liu, C. Chan and P. Sheng, "Three-component Elastic Wave Band-gap Material”, *Physical Review B,* vol. 65, no. 16, pp. 165116, 2002.

34. C. Goffaux and J. Sanchez-Dehesa, "Two-dimensional Phononic Crystals Studied Using a Variational Method: Application to Lattices”, *Physical Review B,* vol. 67, no. 14, pp. 144301, 2003.

35. Y. Jin, X. Jia, Q. Wu, X. He, G. Yu, L. Wu and B. Luo, "Design of Vibration Isolators by Using the Bragg Scattering and Local Resonance Band Gaps in a Layered Honeycomb Meta-structure”, *Journal of Sound and Vibration,* vol. 521, pp. 116721, 2022.

36. Z. Wu, W. Liu, F. Li and C. Zhang, "Band-gap Property of a Novel Elastic Metamaterial Beam with X-shaped Local Resonators", *Mechanical Systems and Signal Processing*, vol. 134, pp. 106357, 2019.

37. T. Wang, M. Sheng and Q. Qin, "Multi-flexural Band Gaps in an Euler–Bernoulli Beam with Lateral Local Resonators", *Physics Letters A,* vol. 380, no. 4, pp. 525-529, 2016.

38. J. Zhou, K. Wang, D. Xu and H. Ouyang, "Local Resonator with High-static-low-dynamic Stiffness for Lowering Band Gaps of Flexural Wave in Beams", *Journal of Applied Physics,* vol. 121, no. 4, pp. 044902, 2017.

39. Y. Xiao, J. Wen and X. Wen, "Flexural Wave Band Gaps in Locally Resonant Thin Plates with Periodically Attached Spring–mass Resonators", *Journal of Physics D: Applied Physics,* vol. 45, no. 19, pp. 195401, 2012.

40. C. Yilmaz, G. M. Hulbert and N. Kikuchi, "Phononic Band Gaps Induced by Inertial Amplification in Periodic Media", *Physical Review B-Condensed Matter and Material Physics,* vol. 76, no. 5, pp. 054309, 2007.

41. C. Yilmaz and G. M. Hulbert, "Theory of Phononic Gaps Induced by Inertial Amplification in Finite Structures", *Physics Letters A* , vol. 374, no. 34, pp. 3576-3584, 2010.

42. M. Hou, J. H. Wu, S. Cao and D. Guan, "Extremely Low Frequency Band Gaps of Beam-like Inertial Amplification Metamaterials", *Modern Physics Letters B,* vol. 31, no. 27, pp. 1750251, 2017.

43. Y. Zeng, L. Cao, S. Wan, T. Guo, Y.-F. Wang, Q.-J. Du, B. Assouar and Y.-S. Wang, "Seismic Metamaterials: Generating Low-frequency Bandgaps Induced by

Inertial Amplification”, *International Journal of Mechanical Sciences*, vol. 221, pp. 107224, 2022.

44. C. Xi, L. Dou, Y. Mi and H. Zheng, "Inertial Amplification Induced Band Gaps in Corrugated-core Sandwich Panels”, *Composite Structures*, vol. 267, pp. 113918, 2021.

45. W. Ding, T. Chen, C. Chen, D. Chronopoulos and J. Zhu, "A Three-dimensional Twisted Phononic Crystal with Omnidirectional Bandgap Based on Inertial Amplification by Utilizing Translation-rotation Coupling”, *Journal of Sound and Vibration*, vol. 541, pp. 117307, 2022.

46. N. Frandsen, O. R. Bilal, J. Jensen and M. I. Hussein, "Inertial Amplification of Continuous Structures: Large Band Gaps from Small Masses”, *Journal of Applied Physics*, vol. 119, pp. 124902, 2016.

47. Y. Li, N. Zhao and S. Yao, "Nonlinear Dynamics of 1D Meta-structure with Inertia Amplification”, *Applied Mathematical Modelling*, vol. 118, pp. 728-744, 2023.

48. V. Gomez-Jauregui, A. Carrillo-Rodriguez, C. Manchado and P. Lastra-Gonzalez, "Tensegrity Applications to Architecture, Engineering and Robotics: A Review”, *Applied Sciences*, vol. 13, no. 15, pp. 8669, 2023.

49. T. E. Sterk, "Using Actuated Tensegrity Structures to Produce a Responsive Architecture”, *ACADIA*, vol. 7, no. 39, pp. 84-92, 2003.

50. W. Gilewski, J. Klosowska and P. Obara, "Applications of Tensegrity Structures in Civil Engineering”, *Procedia Engineering*, vol. 111, pp. 242-248, 2015.

51. H. Furuya, "Concept of Deployable Tensegrity Structures in Space Application", *International Journal of Space Structures*, vol. 7, no. 2, pp. 143-151, 1992.

52. A. S. Mills, *The Structural Suitability of Tensegrity Aircraft Wings*, M.S. Thesis, University of Dayton, 2020.

53. M. Masic, R. E. Skelton and P. E. Gill, "Optimization of Tensegrity Structures", *International Journal of Solids and Structures,* vol. 43, no. 16, pp. 4687-4703, 2006.

54. C. S. Chen and D. E. Ingber, "Tensegrity and Mechanoregulation: from Skeleton to Cytoskeleton", *OsteoArthritis and Cartilage*, vol. 7, no. 1, pp. 81-94, 1999.

55. C. Yilmaz and N. Kikuchi, "Analysis and Design of Passive Band-stop Filter-type Vibration", *Journal of Sound and Vibration,* vol. 291, no. 3-5, pp. 1004-1028, 2006.

56. P. Sui, Y. Shen, S. Yang and J. Wang, "Parameters Optimization of Dynamic Vibration Absorber Based on Grounded Stiffness, Inerter, and Amplifying Mechanism", *Journal of Vibration and Control,* vol. 28, no. 23-24, pp. 3767-3779, 2022.

57. H. Ma, Z. Cheng, Z. Shi and A. Marzani, "Structural Vibration Mitigation via an Inertial Amplification Mechanism Based Absorber", *Engineering Structures*, vol. 295, pp. 116764, 2023.

58. Z. Cheng, A. Palermo, Z. Shi and A. Marzani, "Enhanced Tuned Mass Damper Using an Inertial Amplification Mechanism", *Journal of Sound and Vibration*, vol. 475, pp. 115267, 2020.

59. X. Fang, K.-C. Chuang, X. Jin and Z. Huang, "Band-gap Properties of Elastic Metamaterials with Inerter-based Dynamic Vibration Absorbers”, *Journal of Applied Mechanics*, vol. 85, no. 7, pp. 071010, 2018.

60. L. Li, Q. Wang, H. Liu, L. Li, Q. Yang and C. Zhu, "Seismic Metamaterials Based on Coupling Mechanism of Inertial Amplification and Local Resonance”, *Physica Scripta,* vol. 98, no. 4, pp. 045024, 2023.

61. J. Zhou, L. Dou, K. Wang, X. Daolin and H. Ouyang, "A Nonlinear Resonator with Inertial Amplification for very Low-frequency Flexural Wave Attenuations in Beams”, *Nonlinear Dynamics,* vol. 96, pp. 647-665, 2019.

62. V. G. Jáuregui, *Tensegrity Structures and their Application to Architecture*, Editorial de la Universidad de Cantabria, Santander, 2020.

63. D. S. Shah, J. W. Booth, R. L. Baines, K. Wang, M. Vespignani, K. Bekris and R. Kramer-Bottiglio, “Tensegrity Robotics”, *Soft Robotics,* vol. 9, no. 4, pp. 639-656, 2022.

64. M. Shibata, F. Saijyo and S. Hirai, "Crawling by Body Deformation of Tensegrity Structure Robots”, *IEEE International Conference on Robotics and Automation,* Kobe, Japan, pp. 4375-4380, 2009.

65. C. Paul, . F. J. Valero-Cuevas and H. Lipson, "Design and Control of Tensegrity Robots for Locomotion”, *IEEE Transactions on Robotics,* vol. 22, no. 5, pp. 944-957, 2006.

66. A. G. Rovira and J. M. M. Tur, "Control and Simulation of a Tensegrity-based Mobile Robot”, *Robotics and Autonomous Systems,* vol. 57, no. 5, pp. 526-535, 2009.

67. K. Caluwaerts, J. Despraz, A. Işçen, A. P. Sabelhaus, J. Bruce, B. Schrauwen and V. SunSpiral, "Design and Control of Compliant Tensegrity Robots through Simulation and Hardware Validation”, *Journal of the Royal Society Interface,* vol. 11, no.98, pp. 20140520, 2014.

68. J. W. Booth, O. Cyr-Choiniere, J. C. Case, D. Shah, M. C. Yuen and R. Kramer-Bottiglio, "Surface Actuation and Sensing of a Tensegrity Structure Using Robotic Skins”, *Soft Robotics,* vol. 8, no. 5, pp. 531-541, 2020.

69. L. Rhode-Barbarigos, N. Bel Hadj Ali and R. Motro, "Designing Tensegrity Modules for Pedestrian Bridges”, *Engineering Structures,* vol. 32, no. 4, pp. 1158-1167, 2010.

70. K. Snelson, "The Art of Tensegrity”, *International Journal of Space Structures,* vol. 27, no. 2-3, pp. 71-80, 2012.

71. E. Pontello, R. Maffei and P. Beccarelli, "Design-to-Production Process for Large-Scale Inflated Tensegrity Artwork”, *Proceedings of the IASS 2024 Symposium,* Zurich, Switzerland, pp. 1-10, 2024.

72. H. Lee, J. Kim, N. Lone, J. P. Lee, H. Song, S. Lee, J. K. Cho and Y. Jang, "3D-printed Programmable Tensegrity for Soft Robotics”, *Science Robotics,* vol. 5, no. 45, pp. 9024, 2020.

73. K. Suzumori, H. Nabae and R. Kobayashi, "Large Torsion Thin Artificial Muscles Tensegrity Structure for Twist Manipulation”, *IEEE Robotics and Automation Letters,* vol. 8, no. 3, pp. 1207-1214, 2023.

74. D. E. Ingber, "Tensegrity I. Cell Structure and Hierarchical Systems Biology”, *Journal of Cell Science,* vol. 116, no. 7, pp. 1157-1173, 2003.

75. D. E. Ingber, N. Wang and D. Stamenovic, "Tensegrity, Cellular Biophysics, and the Mechanics of Living Systems”, *Reports on Progress in Physics,* vol. 77, no. 4, pp. 046603, 2014.

76. D. E. Ingber, "Tensegrity II. How Structural Networks Influence Cellular Information Processing Networks”, *Journal of Cell Science,* vol. 116, no. 8, pp. 1397-1408, 2003.

77. D. E. Ingber, S. R. Heidemann, R. E. Buxbaum and P. Lamoureux, "Opposing Views on Tensegrity as a Structural Framework for Understanding Cell Mechanics”, *Journal of Applied Physiology,* vol. 89, no. 4, pp. 1663-1678, 2000.

78. G. Scarr, "Helical Tensegrity as a Structural Mechanism in Human Anatomy”, *International Journal of Osteopathic Medicine,* vol. 14, no. 1, pp. 24-32, 2011.

79. D. Zappetti, S. Mintchev, J. Shintake and D. Florean, "Bio-inspired Tensegrity Soft Modular Robots”, *Biomimetic and Biohybrid Systems: 6th International Conference,* Stanford, CA, USA, pp. 497-508, 2017.

80. Y. Liu, Q. Bi and X. Yue, "A review on Tensegrity Structures-based Robots”, *Mechanism and Machine Theory,* vol. 168, pp. 104571, 2022.

81. J. He, Y. Wang, X. Li, H. Jiang, H. Xie and Y. Zhou, "Minimal Mass Optimization of Tensegrity Torsional Structures”, *Composite Structures,* vol. 345, pp. 118376, 2024.

82. Z. Cao, A. Luo, H. Liu and Y. Feng, "A Novel Torque Application Method for Tensegrity Structures”, *Mechanics Based Design of Structures and Machines,* vol. 52, no. 10, pp. 7864-7885, 2024.

83. G. Sánchez-Arriaga, Á. Cerrillo-Vacas, D. Unterweger and C. Beaupoil, "Dynamic Analysis of the Tensegrity Structure of a Rotary Airborne Wind Energy Machine”, *Wind Energy Science,* vol. 9, no. 5, pp. 1273-1287, 2024.

84. A. H. Orta and Ç. Yılmaz, "Inertial Amplification Induced Phononic Band Gaps Generated by a Compliant Axial to Rotary Motion Conversion Mechanism”, *Journal of Sound and Vibration,* vol. 439, pp. 329-343, 2019.

85. S. Zi-Yan , Y. Xiao-Hui, L. Ao , Y. Xu , G. Zhi-Ying and Z. Li-Yuan , "A Tensegrity-based Torsional Vibration Isolator with Broad Quasi-zero-stiffness Region”, *Mechanical Systems and Signal Processing,* vol. 224, pp. 112215, 2025.

86. N. K. Pham and E. A. P. Hernandez, "Modeling and Design Exploration of a Tensegrity-based Twisting Wing”, *Journal of Mechanisms and Robotics,* vol. 13, no. 3, pp. 031019, 2021.

87. J. Sun, X. Li, Y. Xu, T. Pu, J. Yao and Y. Zhao, "Morphing Wing Based on Trigonal Bipyramidal Tensegrity Structure and Parallel Mechanism”, *Machines,* vol. 10, no. 10, pp. 930, 2022.

88. D. H. Myszka and J. J. Joo, "A Study on the Structural Suitability of Tensegrity Structures to Serve as Morphing Aircraft Wings”, *ASME International Design*

Engineering Technical Conferences and Computers and Information in Engineering Conference, vol. 51814, Quebec City, Quebec, Canada, pp. V05BT07A005, 2018.

89. N. K. Pham and E. A. P. Hernandez, "Design Exploration of a Tensegrity-based Twisting Wing”, *ASME International Design Engineering Technical Conferences and Computers and Information in Engineering Conference*, vol. 83990, Virtual, Online, pp. V010T10A072, 2020.